

Inferring the Andromeda Galaxy’s Mass from its Giant Southern Stream with Bayesian Simulation Sampling

Mark A. Fardal^{1*}, Martin D. Weinberg¹, Arif Babul², Mike J. Irwin³,
 Puragra Guhathakurta⁴, Karoline M. Gilbert^{5,11}, Annette M. N. Ferguson⁶,
 Rodrigo A. Ibata⁷, Geraint F. Lewis⁸, Nial R. Tanvir⁹, Avon P. Huxor¹⁰

¹*Dept. of Astronomy, University of Massachusetts, Amherst, MA 01003, USA*

²*Dept. of Physics & Astronomy, University of Victoria, Elliott Building, 3800 Finnerty Rd., Victoria, BC, V8P 1A1, Canada*

³*Institute of Astronomy, University of Cambridge, Madingley Road, Cambridge CB3 0HA*

⁴*UCO/Lick Observatory, Dept. of Astronomy & Astrophysics, Univ. of California, 1156 High St., Santa Cruz, CA 95064, USA*

⁵*Department of Astronomy, University of Washington, Box 351580, Seattle, WA 98195-1580, USA*

⁶*Institute for Astronomy, University of Edinburgh, Royal Observatory, Blackford Hill, Edinburgh EH9 3HJ*

⁷*Observatoire Astronomique, Université de Strasbourg, CNRS, 11 rue de l’Université, F-67000 Strasbourg, France*

⁸*Sydney Institute for Astronomy, School of Physics, A28, University of Sydney, NSW 2006, Australia*

⁹*Department of Physics and Astronomy, University of Leicester, University Road, Leicester LE1 7RH*

¹⁰*Astronomisches Rechen-Institut, Universität Heidelberg, Mönchhofstrasse 12-14, 69120 Heidelberg, Germany*

¹¹*Hubble Fellow*

Submitted to MNRAS 14 May 2018

ABSTRACT

M31 has a giant stream of stars extending far to the south and a great deal of other tidal debris in its halo, much of which is thought to be directly associated with the southern stream. We model this structure by means of Bayesian sampling of parameter space, where each sample uses an N -body simulation of a satellite disrupting in M31’s potential. We combine constraints on stellar surface densities from the Isaac Newton Telescope survey of M31 with kinematic data and photometric distances. This combination of data tightly constrains the model, indicating a stellar mass at last pericentric passage of $\log_{10}(M_s/M_\odot) = 9.5 \pm 0.1$, comparable to the LMC. Any existing remnant of the satellite is expected to lie in the NE Shelf region beside M31’s disk, at velocities more negative than M31’s disk in this region. This rules out the prominent satellites M32 or NGC 205 as the progenitor, but an overdensity recently discovered in M31’s NE disk sits at the edge of the progenitor locations found in the model. M31’s virial mass is constrained in this model to be $\log_{10} M_{200} = 12.3 \pm 0.1$, alleviating the previous tension between observational virial mass estimates and expectations from the general galactic population and the timing argument. The techniques used in this paper, which should be more generally applicable, are a powerful method of extracting physical inferences from observational data on tidal debris structures.

Key words: galaxies: kinematics and dynamics – galaxies: interactions – galaxies: haloes – galaxies: individual: M31 – methods: statistical.

1 INTRODUCTION

In the current model of structure formation, the stellar halos of galaxies are thought to be messy, inhomogeneous places, populated not only by satellite galaxies and globular clusters but also by tidal debris structures that are mixed to varying degrees (Searle & Zinn 1978; Bullock & Johnston 2005; Abadi et al. 2006; Johnston et al. 2008; Cooper et al. 2010). Observations give strong support to this picture: for exam-

ple, the MW contains numerous streams of stars ripped from dwarf satellites and globulars by the galactic potential. These range from the Sagittarius galaxy’s tidal stream to numerous smaller streams, most of which have no identified progenitor. Our external view of M31 has enabled photometric surveys that give us more complete (though shallower) coverage than is available in the Milky Way. The inhomogeneities there are even more impressive: a 150-kpc-long tidal stream to the south (the giant southern stream or GSS, Ibata et al. 2001, 2007), several tangential streams across the minor axis (Ibata et al. 2007; Chapman et al.

* E-mail: fardal@astro.umass.edu

2008; McConnachie et al. 2009; Tanaka et al. 2010), and numerous structures resembling blobs, spurs, or shelves more than streams (Ferguson et al. 2002; Ibata et al. 2005; Fardal et al. 2007; Ibata et al. 2007; McConnachie et al. 2009). Surveys of more distant galaxies have found additional tidal streams (e.g., Martínez-Delgado et al. 2008, 2009), showing that streams are common features of galaxy halos.

These cold structures are important in their own right: they are the products of hierarchical galaxy formation, and studying the information encoded in their kinematics and chemical composition can lead to insight into the way structure forms on halo mass scales of $\sim 10^{12} M_{\odot}$ down to $\sim 10^8 M_{\odot}$ (Bullock & Johnston 2005; Johnston et al. 2008; Font et al. 2008; Gilbert et al. 2009). They are also significant as kinematic probes of the halo mass, both in the Milky Way (Helmi 2004; Johnston et al. 2005; Grillmair 2009; Willett et al. 2009; Koposov et al. 2010) and in M31 (Ibata et al. 2004; Fardal et al. 2006), though results from this approach are still controversial. While in other galaxies the mass can be estimated by means of satellite tracers (Brainerd & Specian 2003; More et al. 2009), abundance at a given stellar mass (e.g. Yang et al. 2009; Guo et al. 2010; Behroozi et al. 2010), or gravitational lensing (Mandelbaum et al. 2006), these estimates are generally statistical in nature, and thus may gloss over systematic differences between halos of different galaxy types. A well-determined mass profile using cold kinematic tracers in the halo of the MW or in M31 would provide an important test of these techniques. Cold streams could also reveal more subtle aspects such as halo prolateness/oblateness (Helmi 2004; Johnston et al. 2005), triaxiality (Law et al. 2009), or substructure (Johnston et al. 2002; Carlberg 2009). Furthermore, the mass of M31's halo is important for understanding this much-studied galaxy itself, as well as its satellite system, which is fundamental to the study of galaxy formation on small scales.

M31's giant southern stream (GSS) provides one of the best prospects for such a mass determination, because it spans a large range in radius and because its large stellar mass yields many spectroscopic targets. (Various arguments assign its initial stellar mass to be in the range 10^8 to $5 \times 10^9 M_{\odot}$, according to Font et al. 2006.) The stream falls in from behind M31 (McConnachie et al. 2003) and speeds up as it goes (Ibata et al. 2004; Guhathakurta et al. 2006; Kalirai et al. 2006; Gilbert et al. 2009).

Ibata et al. (2004) and Font et al. (2006) attempted to fit progenitor orbits to the stream to determine its orbit and constrain M31's halo mass. However, there are two major problems with this method. The first is that the stream does not coincide with the orbit, as expected on general grounds and shown explicitly with N -body simulations (Fardal et al. 2006). Especially for a highly radial, massive stream such as the GSS, the trailing part of the stream consists of stars boosted to much higher energies than that of the stream progenitor, increasingly so as one goes further out in the stream. As a partial fix, Fardal et al. (2006) found an approximation relating the progenitor orbit to the stream (extending work by Johnston 1998), enabling the central path of the stream through phase space to be estimated without the use of N -body simulations. Even so, the wide range of possible energy boosts rendered estimates of the halo mass

and orbit highly uncertain, and Fardal et al. (2006) could only state that any continuation of the stream must be to the NE of M31's center.

The second problem is that an approximation based on the central path of the stream cannot make effective use of the full debris distribution, especially that of subsequent wraps which may appear as widely dispersed tidal features. In Fardal et al. (2007, henceforth F07), we used N -body simulations to argue that red giant branch (RGB) stars and planetary nebulae (PNe) seen in and around the NE half of M31's disk constituted a second wrap of the orbit, while a faint structure seen to the W side of the disk was a third wrap (see Figure 1). This remarkably successful scenario has received subsequent support from studies of the stellar population in these regions (Richardson et al. 2008), from spectroscopic discovery of the apparent fourth wrap of the orbit (Gilbert et al. 2007), and from measurements of the velocity distribution in the W Shelf region (Fardal et al. 2012). The model can be refined by adding rotation to the progenitor, which improves the transverse profile of the stream (Fardal et al. 2008).

In this paper we seek to improve on the model of F07 by quantitative comparison of simulations and observations. Using simulations to improve and constrain the model is difficult, however. Simulations are slow, and in addition intrinsically stochastic, which presents difficulties for gradient-based fitting techniques and uncertainties based on second derivatives of the likelihood. Therefore, we have chosen to explore parameter space with sampling techniques commonly used in Bayesian statistics. Our approach is related to several prior efforts to automate fitting of merger debris using methods such as genetic algorithms (Theis & Kohle 2001; Howley et al. 2008). However, these efforts have only sought a best-fit model of merger debris without quantifying the parameter uncertainties. Our goal here is to *sample the full parameter distribution*, in order to draw scientifically useful conclusions (i.e., with uncertainty estimates) about interesting issues such as the mass of the progenitor and of M31's halo. The combination of Bayesian sampling with N -body simulations of specific structures has not been tried before to our knowledge, and one might expect a very large number of N -body simulations would be required. This paper therefore serves among other purposes to test whether the method is currently feasible.

The rest of the paper starts by describing in Section 2 our methods for sampling from parameter space. We begin with a sketch of the procedure before plunging into the details. We then describe the physical collision model and its parameterization, the likelihood function which incorporates constraints from star-count maps as well as velocity and distance measurements along the GSS, and the method used to sample from parameter space. Section 3 presents our results, in terms of both the distributions of the model parameters and of the GSS debris structures generated by the simulation samples. We find tight constraints on most of our parameters, including M31's halo mass, and significant correlations among some of them. We illustrate both the characteristic features and the variable aspects of the simulations, test the goodness of fit of the models, check their validity using observables not included in the likelihood function, and offer predictions for future observations. Section 4 discusses

various aspects of this work, and Section 5 summarizes the paper.

2 METHODS

2.1 Overview

For reasons that will soon be apparent, a full description of our analysis methods will be rather complex, so we begin by describing its most essential aspects. Let us first summarize the model in F07. This starts with a satellite galaxy of a certain mass and density profile, moving in a potential specified by parameters for M31's baryonic and dark components, on a certain orbit which happens to be highly radial. After its first pass through pericenter, its stars disperse onto orbits with a wide range of energies, which spread and form structures resembling the GSS, NE Shelf, and W Shelf features in M31. (See Figure 1, and compare the simulations in Figure 4 which have similar sky patterns to that in F07.) This single model is qualitatively quite successful, as it simultaneously explains many separate features in detail and has made several successful predictions (see Gilbert et al. 2009; Fardal et al. 2012). At the same time, there are quantitative aspects that could be improved, particularly the velocity of the GSS.

The F07 model is simple enough to be described just by the parameters listed in Table 2 of that paper. Some of these are not of any fundamental interest, like the exact starting point and speed of the satellite. Others are more significant, such as those describing the gravitational potential of M31. We can think of the F07 model as a single point in a low-dimensional parameter space. We would like to know, is there a better model somewhere in the space? And where do the allowable models live; more precisely, what is the full probability distribution in this parameter space?

Bayesian statistics gives us a means of answering these questions, at the cost of supplying four separate ingredients. The first ingredient, which we already have, is a model parameter space containing parameter vectors \mathbf{M} . The next is a prior probability distribution $P(\mathbf{M})$ on this parameter space, which takes into account information beyond that incorporated in the particular measurement we are making. For example, M31's gravitational potential is not known precisely, but we can try to quantify its probability distribution based on observables that have nothing to do with the GSS. The next ingredient is the likelihood function $\mathcal{L} = P(\mathbf{D}|\mathbf{M})$, the probability distribution of the GSS-related data given the model. In our case this needs to be calculated by performing a simulation with the given parameters, then comparing this simulation to data in a quantitative way. Using Bayes's theorem, we can write the final (or posterior) probability distribution $P(\mathbf{M}|\mathbf{D})$ of the parameters as the product of the prior and likelihood functions:

$$P(\mathbf{M}|\mathbf{D}) = \frac{P(\mathbf{D}|\mathbf{M})P(\mathbf{M})}{P(\mathbf{D})} \quad (1)$$

(In this paper we will generally regard $P(\mathbf{D})$ as an uninteresting normalization constant.) The final ingredient in Bayesian statistics is an effective means of sampling parameter vectors from the posterior probability distribution, in order to describe the distribution accurately. As is often the case, we supply this using a particular form of Markov Chain

Monte Carlo (MCMC) sampling. Having finally produced a sample of parameter vectors, we can manipulate it in many ways to obtain physical information. For example, we can compute the marginal distribution for each of the individual parameters, or for any quantity of interest that can be computed from them.

This paradigm of Bayesian sampling is probably familiar to most readers. There are some special features in our case, though, that will make our procedure quite detailed and difficult. One is obvious: performing an N -body simulation at each likelihood evaluation is rather slow. Even if we sample using MCMC methods rather than a brute-force grid search, and split the calculation into chains run in parallel, we still expect the sampling will take hundreds or thousands of steps at a minimum. So we will need to perform the sampling efficiently to have any hope of success. We also aim to keep the model space as simple as possible, since sampling the distribution becomes more difficult when more parameters are added.

Other difficulties arise from the particular problem studied here. For example, we need to combine a set of different types of observations to effectively constrain the model, and for each type we explain in detail how we quantify its contribution to the likelihood function. In addition, we must be careful about which observations *not* to include, either because we believe they are contaminated by other components beyond hope of recovery, or because we expect they cannot be reproduced effectively by our simple models. Complicating things further, we intend to use several parameter spaces of different dimension, in order to understand the effects of various parameters and the robustness of our results.

Furthermore, there is one feature of our sampling problem that seems unusual, at least in an astronomical context. Our likelihood function is based on a particle simulation, and therefore is *intrinsically* stochastic, significantly so in our case.¹ There is a true value of the model likelihood that would be obtained with a large number of simulation particles, but the likelihood value we obtain is randomly scattered around it. If we repeat the simulation, using a different random seed to initialize the satellite particles, we will get a different value for the likelihood function. We discuss the effect of this stochasticity or "likelihood noise" in Section 2.5.2 and suggest several rules of thumb for dealing with it. The one to remember for now is that we should try to keep the number of observational constraints as low as possible, consistent with the requirement that we effectively constrain the posterior distribution.

In the rest of this section we fill in the details of our procedure. (The reader not interested in details might be well-served to glance at Figure 1 and Tables 1–4, and then skip to Section 3.) In Section 2.2 we describe our collision model, including the initial structure of the satellite, the or-

¹ Even though our approach involves approximate Bayesian computation, it should not be confused with the so-called Approximate Bayesian Computation method (e.g., Beaumont 2010). This latter approach dispenses with the mathematically formulated likelihood altogether, and instead samples from parameter space while requiring that a full simulation of the data values, including observational errors, lie close (in some predefined sense) to the observed data values.

bitial initial conditions, and our methods for initializing and evolving the system in an automated way. We also describe our quasi-analytic approximation for the stream’s central path, which will be used in several parts of the likelihood function. We specify in Section 2.3 several related model parameter spaces from which we will draw samples, and the priors on the parameters. In Section 2.4, we then discuss the different types of observational data used, and how we compare to these to form the various terms in the likelihood function. Section 2.5 describes our procedures for sampling from the posterior probability distribution, including methods to help deal with noise in the likelihood function. Finally, we describe in Section 2.6 the actual MCMC runs generated using these procedures.

2.2 Collision model

Each of our parameter evaluations starts by setting up a self-gravitating N -body model of a satellite in a fixed potential model mimicking that of M31, infalling from near apocenter. We then follow its evolution with an N -body code for a time prescribed by the orbital parameters. Our basic scenario (as in F07) specifies that as one follows the stream material forward in its path, it forms the GSS region, NE Shelf, and W Shelf (see Figure 1) from three successive orbital wraps.

Here we use a spherical Plummer model for the satellite. This is an extremely simple model, which nevertheless provides a reasonable fit to many real low-mass galaxies (McConnachie & Irwin 2006). In Fardal et al. (2008) we studied the effect of a flattened rotating progenitor, finding the final overall morphology was generally similar. However, there are some subtle differences from a spherical model, chief among them the skewed transverse distribution of stars in the GSS. Later we will design the likelihood function to be insensitive to this skew. For the purposes of this paper, the simplicity of the spherical model outweighs anything to be gained by using a more complex rotating model.

Real galaxies should have at least two differently distributed components, stars and dark matter, and perhaps a gas component as well. However, the stars in the GSS are almost entirely > 4 Gyr old with a typical age of ~ 8 Gyr, as found by modeling of HST/ACS data on the GSS down to the main sequence in Brown et al. (2006). This suggests there has been little gas in the satellite for some time. This lack of gas might be related to the length of time the satellite has spent in M31’s halo. A typical apocenter for the GSS progenitor of ~ 50 kpc, as found in F07, is also inconsistent with a very recent accretion from outside the virial radius. Therefore we expect that much of the progenitor’s dark matter will have been stripped off in orbits prior to its most recent collision, consistent with trends found in cosmological simulations (Libeskind et al. 2011). We thus find it both reasonable and convenient to assume a single M/L ratio throughout the satellite. To us it seems equally plausible that the mass should be dominated by stars or dominated by dark matter, and we consider two models, one where we fix M/L and one where we leave it free to vary. Mori & Rich (2008) have considered a GSS progenitor with a massive halo, finding that a total satellite mass of $\lesssim 5 \times 10^9 M_{\odot}$ is required to avoid perturbing M31’s disk too much. We will find later that much of the mass allowed by this limit will be taken up by stars, leaving little room for a dark halo.

We create the initial satellite particle distribution with the library ZENO by Josh Barnes. This solves the Abel integral to compute the exact velocity distribution for the specified density model, enabling rapid production of accurate equilibrium initial conditions for any initial profile, though in this paper we restrict ourselves to the Plummer profile which has an analytic solution. We use 65,536 particles in each satellite, as a compromise between the competing demands of computation time and simulation noise (see the discussion in Section 2.5). Tests with an isolated satellite show minimal evolution over the typical duration of the run. Each simulation uses a different random number seed, and thus a different distribution of particles even for identical parameters.

We omit dynamical friction from the calculation. In earlier test simulations with live halos and disks and analytic approximations, we found that the main effect of dynamical friction in reasonable models is to induce a loss of energy at the first pericentric passage, when the satellite is still intact. This means the orbit should actually be started at a slightly higher energy, but otherwise the structure is little affected. It would be impractical to conduct a large number of simulations with a full N -body model for the primary. Analytic approaches can provide at least an estimate of the drag on the satellite, but it is difficult to accurately calculate the force field that should be applied to the entire tidal structure. In addition, it simplifies the analysis to be able to speak of fixed orbital quantities such as the apocenter. Therefore we postpone consideration of dynamical friction to future work.

In some tidal stream problems it is convenient to simplify the problem even further using a reduced N -body model, i.e. fix the satellite potential and follow the evolution of massless test particles. However, in our case the self-gravity is essential. Clearly the satellite is largely ripped up by its encounter, so the time variation in its potential has a major effect on the final debris. Comparison of full and reduced N -body calculations show a large difference in the stream’s surface density in particular. Since the stellar surface density will be one of the primary observables, it is essential to use a live satellite despite the extra computational burden.

We set up a fixed M31 potential consisting of a bulge, disk, and halo, where the parameters controlling this potential are described in more detail later. We follow the satellite’s evolution with PKDGRAV, a versatile multi-stepping tree code written by Joachim Stadel and Tom Quinn (Stadel 2001). We have customized this code to accept parameters for our fixed potential components. We choose a spline softening length equal to 0.3 times the Plummer scale radius. We also use fourth-order multipoles in the node potential expansions, set the opening angle to $\theta = 0.8$, and use the acceleration-based timestepping criterion with $\eta_{acc} = 0.2$.

2.2.1 Orbital approximation

As mentioned before, the orbit of the GSS progenitor is a very poor approximation to the resulting stream (Fardal et al. 2006), but it is possible to find an approximation of the central path of the stream in phase space. The most useful approximation in the current case, where the orbit is highly radial and the progenitor disrupts al-

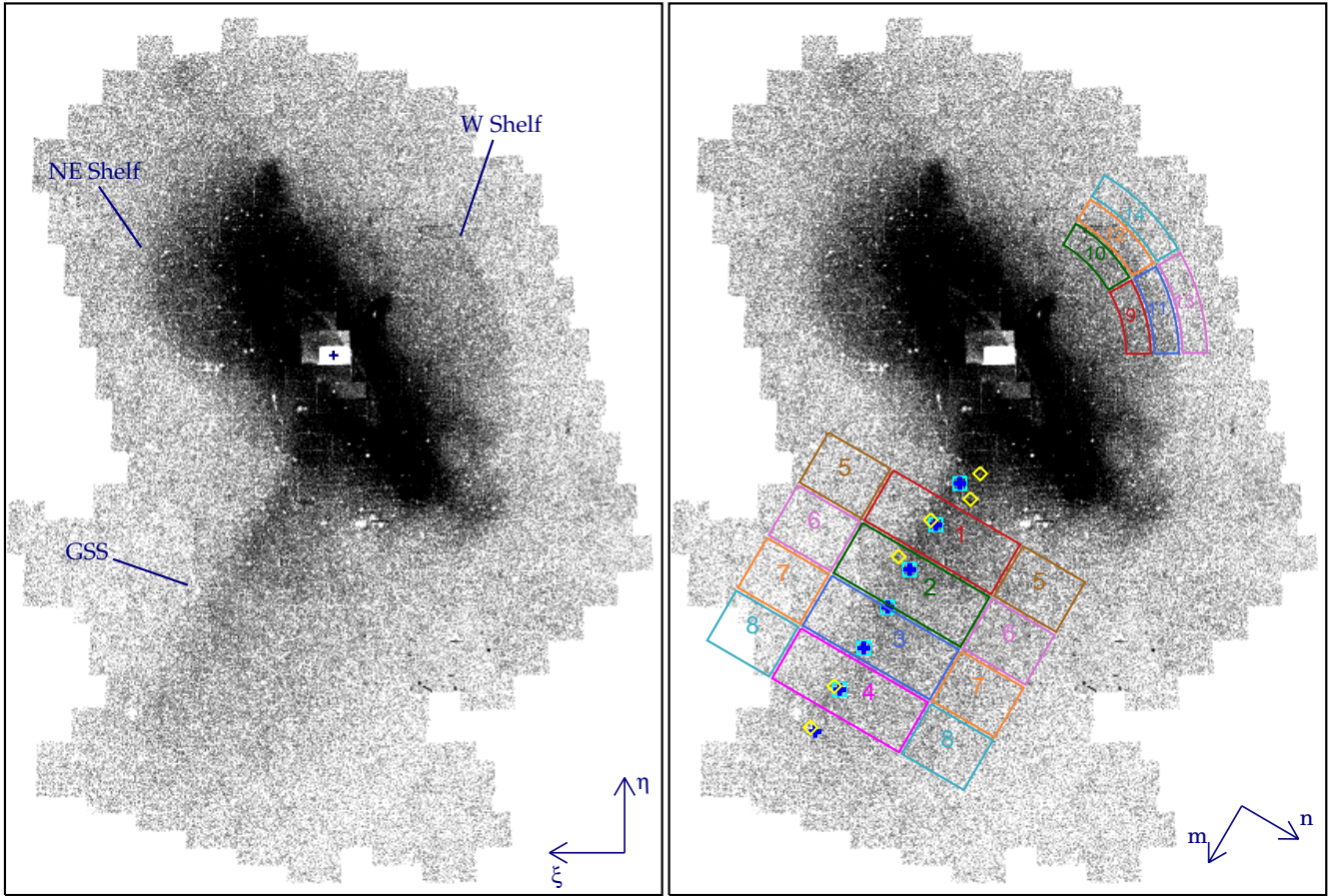


Figure 1. Left panel: map of the RGB count density around M31 from the INT survey. Pixel intensities show on a logarithmic scale the number of bright red RGB stars within the color-magnitude cut described in the text. The main morphological features used to constrain the GSS model are indicated, and M31's center marked with a cross. Right panel: same map, but showing regions used to constrain the likelihood function. Outlines with numbers indicate the regions used to compare the observed count density to mass surface densities in the simulations. The “outrigger” regions in the GSS are split to either side of the “central” regions. Squares show the positions used for the central path of the stream, which are barely offset from the field centers of McConnachie et al. (2003). Central positions of fields used for other stream measures are shown by crosses for distances, and diamonds for stream velocities. The maps use a tangent-plane projection centered on M31 with pixels 1 arcmin on a side. They cover a range 3.5 deg to -3.5 deg in ξ , and -5.75 deg to 3.75 deg in η , i.e. approximately $95\text{ kpc} \times 130\text{ kpc}$. Axes at lower right in each panel show the orientations of the sky-aligned ξ - η system and the GSS-aligned m - n system used in the paper.

most completely at pericenter, remains that of Fardal et al. (2006), which relies on scaling the orbit to obtain a track of the stream. While we now wish to use simulations to compare to observations, this “stream-orbit” approximation, so called because it directly relates the progenitor orbit to the path of the stream, remains useful in several respects. First, we can construct a likelihood function based entirely on a single orbital calculation and then sample the resulting probability distribution with standard Bayesian techniques. The resulting “orbital” sample will not reflect all the observational constraints, but will be useful as a starting point for the simulation-based sampling chains. Second, since noise in the likelihood function will prove to be an important factor, we will actually use the orbital model in place of the noisy simulations to estimate several of the stream quantities when computing the full, simulation-based likelihood.

The stream locus in phase space is obtained by first calculating the progenitor's trajectory, assuming it behaves as a test particle in the potential of M31, then analytically distorting it. The orbit is described by position $\mathbf{r}_p(t)$ and ve-

locity $\mathbf{v}_p(t)$. We assume that the potential of M31 is roughly spherical and close to a power-law $\Phi \propto r^k$. In Fardal et al. (2006) we assumed a constant exponent $k = -0.4$, significantly steeper than an isothermal halo. Here, we instead calculate k from the ratio of the gravitational force at 15 and 45 kpc. Given our adjustable potential, this change leads to better agreement with the simulated velocities. For a range of values of M_{200} from 7×10^{11} to $3 \times 10^{12} M_\odot$, this value ranges from -0.4 to $+0.1$.

We assume that the stars in the stream were all liberated at the first pericentric passage, an assumption valid for a highly radial orbit, and set $t = t_d$ at this point. Then we assume that the different stars in the stream have orbits that are geometrically similar but scaled in orbital period by a factor τ . Constructing an array of τ values over some large range, we can then construct a parametric solution of the stream locus at time t by setting the position to $\mathbf{r} = \tau^{2/(2-k)} \mathbf{r}_p[(t - t_d)/\tau]$, and the velocity to $\mathbf{v} = \tau^{k/(2-k)} \mathbf{v}_p[(t - t_d)/\tau]$ (see Fardal et al. 2006).

When we later obtain actual simulations drawn from

various parameter samples, we find good overall agreement between the simulations and the stream-orbit model. Later we discuss slight correction terms we include to improve the model for quantities used in the likelihood function.

2.3 Model parameters and priors

Our goal in constructing the collision model has been to include parameters that have a large effect on the results, while keeping the dimensionality low. To test the significance of different parameters, we define five different parameter spaces in this paper, called the “stellar”, “DM”, “orbital”, “reduced”, and “density” spaces. The parameters used in these model spaces are summarized in Table 1. We begin by discussing the two largest dimension spaces, “stellar” and “DM”, which are the main spaces used for science results. As each parameter is introduced, we discuss its prior probability distribution; these priors are summarized in Table 2.

We state our orbital parameters in a Cartesian coordinate system centered on M31 and aligned with the sky, although the actual calculation uses a rotated system aligned with M31’s disk. The sky system is chosen so that X increases with right ascension to the E, Y increases with declination to the N, and Z increases with distance from Earth. It is simple to translate these into the tangent plane coordinates ξ and η (aligned with X and Y respectively), distance d , and velocity v_r (see Fardal et al. 2006).

The orbital initial conditions require six free parameters. As in previous papers, we choose one of these to be the orbital phase of the progenitor at the present day. We express this phase F_p in terms of the time since the initial disruptive pericentric passage (at t_d) in units of the progenitor’s radial period t_r , so that $F_p = (t - t_d)/t_r$. Models with similar F_p tend to resemble each other except for differences in orientation and scale. In our scenario, $F_p = 0$ represents the initial disruption point, $F_p = 1$ implies the progenitor has just completed the GSS part of the orbit, $F_p = 2$ means it has just moved out to the NE Shelf and back to pericenter, and $F_p = 3$ means it has just completed the W Shelf part of its orbit and returned to pericenter. Since observations suggest that the stream density rises towards the NE Shelf and falls off again in the W Shelf, we assume limits of 0.8 to 2.0. We take the prior on F_p to be uniform within these limits since the disruption time is arbitrary. Note the limits for all parameters are given in Table 2.

With the addition of F_p , we then have one spare phase-space parameter, so we calculate the orbit from a fixed plane $Y_0 = -10$ kpc, which will lie within the GSS orbital wrap. We then calculate the orbit forward and backward from this reference point. The other parameters X_0 , Z_0 , V_{X0} , V_{Y0} , and V_{Z0} are all set to have uniform priors, inside a box placed loosely around values from earlier successful models rather than from any physical considerations. We set $V_{Y0} > 0$ at this reference point so that it corresponds to an upward-moving satellite at a time later than t_d , moving like the stars in the GSS. The satellite itself is started at a much earlier point, just after apocenter on the previous orbital wrap at a time before t_d .

In all except our “density” parameter space, we scale the Plummer scale length of the initial satellite according to $a = 0.8 \text{ kpc} (M_{sat}/10^9 M_\odot)^{1/3}$, so that the central density is fixed at $\rho_{sat} = 4.6 \times 10^8 M_\odot \text{ kpc}^{-3}$ and the central sur-

face density at $5.0 \times 10^8 M_\odot \text{ kpc}^{-2} (M_{sat}/10^9 M_\odot)^{1/3}$. This agrees well with relations for local galaxies (Dekel & Woo 2003; Woo et al. 2008). The mass M_{sat} of the satellite is taken to have a uniform prior in its logarithm, from $10^{8.5}$ to $10^{10} M_\odot$ in our “stellar” model, and over a larger range from $10^{8.5}$ to $10^{11} M_\odot$ in our “DM” model.

We use the bulge-disk-halo potential model of Geehan et al. (2006). The model contains a spherical Hernquist bulge, exponential or Miyamoto disk, and spherical Navarro, Frenk, and White (NFW) halo. As used here, this is a single-parameter family of potentials (the vertical line in Figure 6 of Geehan et al. 2006), with the single degree of freedom mostly controlling the outer halo potential. Two parameters in this model (bulge radius, disk scale length) are well constrained, and we have fixed them at their best-fit values: $r_b = 0.61$ kpc, $r_d = 5.40$ kpc. The classic disk-halo degeneracy is a major degree of freedom in the model; to resolve this we assume a central disk surface density of $4.0 \times 10^8 M_\odot \text{ kpc}^{-2}$, corresponding to a disk mass of $M_d = 7.34 \times 10^{10} M_\odot$ and $(M/L_R)_d = 3.3$. This model also contains a great deal of flexibility in the halo potential because it is constrained only by relatively few statistical tracers, namely PNe, globular clusters, and satellite galaxies combined according to the Bayesian modeling of Evans & Wilkinson (2000) and Evans et al. (2000). Within the code we parameterize the halo’s mass and scale radius r_h by $f_h = r_h/7.9$ kpc, since 7.9 kpc was the scale radius with the highest likelihood at our chosen surface density (Geehan et al. 2006). (In Fardal et al. 2006 we used an earlier version of the Geehan et al. 2006 model based on slightly different data, leading to a maximum likelihood value for r_h of 9.0 kpc.) To within a few percent, the best-fitting bulge mass and halo density parameter along this path are then given by

$$\begin{aligned} M_b &= (3.24 + 0.238u - 0.103u^2 + 0.0158u^3) \times 10^{10} M_\odot, \\ \delta_c &= \exp(12.66 - 1.956u + 0.143u^2), \end{aligned}$$

with $u \equiv \ln f_h$. The halo density parameter in turn sets the dark matter NFW density profile according to $\rho_h(r) = \delta_c \rho_c x^{-1} (x+1)^{-2}$, where $x = r/r_h$ and $\rho_c = 140 M_\odot \text{ kpc}^{-3}$ is the present-day critical density for our assumed Hubble parameter $H_0 = 71 \text{ km s}^{-1} \text{ Mpc}^{-1}$.

In this paper we report the halo mass in terms of the “virial mass” estimator M_{200} , the mass inside a sphere containing an average density 200 times the closure density of the universe. We choose this threshold in preference to M_{100} , also commonly adopted, because of its closer relationship to the length scales actually probed by the GSS. In our model the relationship of this to f_h is described well by

$$\begin{aligned} \log_{10}(M_{200}/M_\odot) &= 11.572 + 0.324f_h - 0.0481f_h^2 \\ &\quad + 0.00438f_h^3 - 0.000159f_h^4. \end{aligned}$$

Since speed is paramount in our case, we have slightly altered the model to use a Miyamoto-Nagai instead of an exponential disk, with $M_{miya} = 1.1M_{exp}$ and $R_{miya} = 1.1R_{exp}$, and disk scale height $b_{miya} = 0.4$ kpc. This slightly changes the total mass by an amount well within the uncertainty, and otherwise seems to give good agreement with the exponential disk forces at most positions.

We incorporate prior knowledge of the M31 halo potential into our calculation. The simple observation that

Table 1. Parameter spaces

Model space	Parameters
“stellar”	$X_0, Z_0, V_{X0}, V_{Y0}, V_{Z0}, F_p, M_{200}, M_{sat}$
“DM”	$X_0, Z_0, V_{X0}, V_{Y0}, V_{Z0}, F_p, M_{200}, M_{sat}, M_{lum}$
“orbital”	$X_0, Z_0, V_{X0}, V_{Y0}, V_{Z0}, F_p, M_{200}$
“reduced”	F_p, M_{200}, M_{sat}
“density”	$F_p, M_{200}, M_{sat}, \rho_{sat}$

$X_0, Y_0, Z_0, V_{X0}, V_{Y0},$ and V_{Z0} denote the phase space coordinates of the reference point in the progenitor’s orbit. The orbital coordinate Y_0 is held fixed at -10 kpc, so it is not a free parameter. F_p is the current orbital phase of progenitor on it by its initial orbit, expressed as the time since its disruptive pericentric passage in units of the radial period. M_{200} is the halo mass of M31, measured within a radius where the mean enclosed density equals 200 times the critical density of the universe. M_{sat} is the initial mass of the progenitor satellite, and M_{lum} its initial luminous mass in the model where these differ. Finally, ρ_{sat} is the central mass density of the progenitor satellite.

Table 2. Parameter priors

Parameter	Minimum	Maximum	Distribution
X_0 (kpc)	-15	20	uniform
Z_0 (kpc)	1	50	uniform
V_{X0} (km s $^{-1}$)	-200	-10	uniform
V_{Y0} (km s $^{-1}$)	10	380	uniform
V_{Z0} (km s $^{-1}$)	-380	-100	uniform
F_p	0.8	2.0	uniform
$\log_{10}(M_{200}/M_{\odot})$	11.80	12.67	peaked, see text
$\log_{10}(M_{sat}/M_{\odot})$	8.5	10.5	uniform (“stellar”)
$\log_{10}(M_{lum}/M_{\odot})$	8.5	11.0	uniform (“DM”)
$\log_{10}(M_{lum}/M_{sat})$	-1.0	0.5	uniform

M31 has baryonic mass $\sim 10^{11} M_{\odot}$ already introduces a fair amount of prior knowledge. Taking into account both the cosmic distribution of galactic halos ($dN/d\ln M_{200} \propto M_{200}^{-0.8}$ in this mass range) and fairly generous limits on the halo mass required to assemble this amount of baryons into a galaxy, we adopt a Gaussian prior for $\log_{10}(M_{200}/M_{\odot})$ with mean 12.2 and dispersion 0.4 dex, which gives a FWHM of almost 1 dex. We then multiply this by the likelihood value from the Geehan et al. (2006) model to form our final prior on M_{200} . The Geehan et al. likelihood factor is quite strongly discouraging of large halo values, dropping to 0.1 of its maximum value already at $\log_{10}(M_{200}/M_{\odot}) = 12.1$ and declining exponentially with scale length 0.08 dex at higher values. However, our previous experience suggests that a good fit to the GSS debris is likely to be found for $f_h > 1$, so we restrict the run to the range $f_h = 0.8-8$, or $M_{200} = 0.63-4.7 \times 10^{12} M_{\odot}$. Purely for technical reasons, within our code we have specified the prior as a flat distribution in f_h and moved the remaining factors to the likelihood. Since the code ultimately samples from the posterior (product of prior and likelihood), this modification has no consequence for our results. The prior distribution on M_{200} can be seen in the inset of Figure 3; it is strongly biased to lower values, whereas the posterior obtained from our MCMC results will have a very different mean.

This completes the specification of our “stellar” model space, which assumes the satellite’s mass is entirely stellar in

nature. For our “DM” model, we draw a distinction between the luminous (stellar) mass M_{lum} and the total mass M_{sat} , which we assume to be blended with (though not necessarily dominated by) dark matter. We parameterize this by the ratio M_{lum}/M_{sat} , for which we take a flat logarithmic prior, and we allow this to vary over a large range (even to values above 1, to see if the observations suggest an error in our mass calibration derived later).

As mentioned earlier, we define an “orbital model” which is based only on the stream-orbit calculations of Section 2.2.1. Since the satellite mass or debris distribution is not considered in this model, the “orbital” space is equivalent to the “stellar” space with satellite mass omitted.

We also consider a “reduced” parameter space, where we eliminate all orbital parameters except for the orbital phase F_p . Here we use the orbital model to compute the maximum-likelihood value of the other orbital parameters $X_0, Z_0, V_{X0}, V_{Y0},$ and V_{Z0} , over a grid of F_p and M_{200} . This leaves a three-dimensional space of $F_p, M_{200},$ and M_{sat} , which can be sampled more easily than our standard model. We used this space for testing purposes while working towards the larger-dimensional results.

Finally, we defined a “density” space, an augmented version of the “reduced” space in which the central density of the progenitor’s Plummer model $\rho_{sat} = (3M_{sat})/(4\pi a^3)$ was left free to vary. We imposed a Gaussian prior on $\log_{10} \rho_{sat}$ with mean -0.3 dex, consistent with the fixed value in our main samples, and dispersion 0.5 dex. We used this space later to test the influence of adding a freely varying satellite size scale, without the computational burden of the full parameter space.

2.4 Likelihood function

Now that we have explained how we go from a point in parameter space to an N -body debris structure, we need to specify the likelihood function, the probability of drawing the data from this debris structure given the N -body model regarded as a function of the model parameters. Because M31 is a highly inhomogeneous environment with many overlapping structures, we try to use only the parts of the data that are least contaminated by unrelated material. As mentioned earlier, each term in the likelihood function that is calculated from the simulation adds noise or stochasticity to the likelihood. Thus it is helpful to keep the number of terms using the simulation on the low side, while still aiming at a combination of data that will constrain the model.

Rather than the true likelihood $\mathcal{L}(D|M)$ (where D means data and M means model), it is usually easier to work with its logarithm $L(D|M) = \ln(\mathcal{L})$. This log-likelihood is comprised of several terms corresponding to different types of GSS observations. Some of these terms were previously used in the orbital fitting of Fardal et al. (2006) and F07, though we have slightly updated the data values:

- L_{pos} , which constrains the central position of the GSS;
- L_d , which specifies the distance of the GSS;
- L_v , which specifies the velocity of the GSS;
- L_{lobe} , which loosely describes the position of the NE shelf.

To this we have grafted on

- L_{im} , which describes the surface density pattern of

Table 3. Observational data

Field	ξ	η	Mean	Error	Reference
Stream transverse coordinate n (degrees)					
F2	1.68	-3.56	0.34	0.20	McConnachie et al. (2003)
F3	1.43	-3.12	0.34	0.20	and see text
F4	1.17	-2.68	0.34	0.20	
F5	0.94	-2.28	0.34	0.20	
F6	0.66	-1.80	0.34	0.20	
F7	0.40	-1.37	0.34	0.20	
Stream distances (kpc), large to small radius					
F1	1.94	-4.01	886	20	McConnachie et al. (2003)
F2	1.68	-3.56	877	20	
F3	1.43	-3.12	860	20	
F4	1.17	-2.68	855	20	
F5	0.94	-2.28	840	20	
F6	0.66	-1.80	836	20	
F7	0.40	-1.37	829	20	
Stream velocities (km s ⁻¹), large to small radius					
s1	1.99	-3.97	-18	25	Ibata et al. (2004)
s2	1.74	-3.52	-45	25	Ibata et al. (2004)
a3	1.06	-2.14	-141	8	Gilbert et al. (2009)
s6	0.71	-1.76	-181	25	Ibata et al. (2004)
H13s	0.29	-1.53	-190	8	Gilbert et al. (2009)
f207	0.19	-1.26	-224	10	Gilbert et al. (2009)

Table 4. INT image data

Region	Raw counts	Background counts	Background error	Area
 (counts arcmin ⁻²)		(arcmin ²)
1	3.49	1.54	0.13	3744
2	2.58	1.19	0.09	3744
3	2.12	0.98	0.03	3744
4	1.76	0.91	0.05	3744
5	1.72	1.44	0.10	3744
6	1.42	1.17	0.07	3744
7	1.31	0.99	0.05	3744
8	1.30	0.94	0.06	3744
9	3.29	2.18	0.27	848
10	3.20	2.09	0.25	848
11	2.47	1.69	0.15	1018
12	2.49	1.71	0.16	1018
13	1.35	1.54	0.14	1188
14	1.59	1.59	0.13	1188

Regions are indicated in Figure 1.

stream material in the GSS and W shelf regions, as based on the image in Figure 1.

All the terms in our likelihood happen to be of the χ^2 form, with $\mathcal{L}_i \propto \exp[-\Sigma_i(D_i - M_i)^2/(2\sigma_i^2)]$, so that $L = -\chi^2/2$ with $\chi^2 \equiv \Sigma_i(D_i - M_i)^2/\sigma_i^2$ for independent data points, or $\chi^2 \equiv (\mathbf{D} - \mathbf{M})\mathbf{C}^{-1}(\mathbf{D} - \mathbf{M})$ for covariant data points where \mathbf{C} is the covariance matrix.

2.4.1 Surface density

To constrain the surface density of GSS debris, we use the Isaac Newton Telescope (INT) *Wide-Field Camera* survey

of M31’s halo in Johnson V and Gunn i filters (Ibata et al. 2001; Ferguson et al. 2002; Irwin et al. 2005). This survey is deep enough to reach $M_V \approx 0$ on the RGB for stars in M31. Details of the photometric pipeline and morphological classification are described in Irwin & Lewis (2001). Color-magnitude cuts in the survey catalog are effective in picking out M31 RGB stars and revealing smooth and structured components of M31’s halo, although foreground Milky Way halo and disk stars and background galaxies are both still major contaminants. The deeper and broader PAndAS survey (McConnachie et al. 2009) (which builds on the quadrant surveyed earlier by Ibata et al. 2007) recently finished acquiring data, but final analysis of the dataset is still ongoing. Fortunately, the INT survey has enough source counts to strongly constrain our models.

The GSS is known to be relatively metal-rich, and therefore most easily visible in red RGB stars, as seen in the map of Irwin et al. (2005). However, the metallicity distribution within the stream is fairly broad (Ibata et al. 2007), so that it is also apparent in the corresponding map of lower-metallicity blue RGB stars in Ferguson et al. (2002). Therefore we use a color cut that is slightly broader than in Irwin et al.’s “red” RGB sample. We first deredden the source magnitudes for Galactic extinction to V_0, i_0 according to Schlegel et al. (1998). We then use cuts of $21 < i_0 < 22$, $V_0 - i_0 > 1.30 + 0.35(22 - i_0)$, representing a compromise between maximizing source counts and excluding unrelated lower-metallicity structures. We include only sources with magnitude uncertainties less than 0.25, and classified as “stellar” or “probably stellar” by the survey pipeline. Published INT maps show square artifacts from field-to-field variations, presumably due to the effect of seeing variations on source detection and star/galaxy separation. A significant fraction of sources satisfying the i magnitude cut have no detection in V , and these show the same square artifacts. We include these sources in our count map weighting each by 50%, as we found that produced smoother maps compared to either including or excluding them entirely. After mapping sources onto a tangent-plane projection and binning into 1 arcmin square pixels, we obtain the star-count map shown in the left panel of Figure 1.

In our scenario for the GSS’s formation, we expect that moving the core forward in its orbit (i.e. increasing the progenitor phase F_p) will cause the surface density in the GSS to decrease, while the opposite is true for the W Shelf which lies ahead of the core (as long as $0.8 < F_p < 2.0$). In F07 we suggested that the ratio of surface brightness in the GSS and W Shelf would make a good constraint on F_p . Here we put this idea into practice. We also use the star-count map to limit the width of the simulated GSS, which relates to its mass and the impact parameter of the orbit.

We choose a set of bins on the sky to satisfy these goals, while avoiding regions like the NE Shelf that are mixed with M31’s disk (see Figure 1, right panel). We set up a rectangle covering the GSS region, slice it in four pieces lined up along the stream, then cut each slice into one central and two “outtrigger” bins so that the central bin contains 50% of the slice’s area. The range along the stream is chosen to avoid both the outer regions where the GSS signal is very faint, and the inner regions that for some parameter settings are covered by the NE Shelf orbital wrap. We anticipate from our work on rotating GSS progenitors (Fardal et al.

2008) that the spherical, non-rotating progenitors used here will have difficulty matching the skewness of the transverse distribution. Therefore we combine the counts of the satellite regions on each side of each central region to form a single bin. To first order this should be unaffected by skewness of the transverse distribution.

In the W Shelf we use three thin radial cuts, with the central one containing the visible W Shelf edge, each split down the middle into two bins to loosely constrain the shelf's azimuthal position. Therefore, in addition to measuring the overall count level and the ratio of GSS to W Shelf counts, the overall combination of 14 bins also measures the gradient of surface density in the GSS, the width of the GSS, and the location of the W Shelf.

We now need to obtain the data values in each bin. We boxcar smooth the star-count map with a window 20 arcmin on a side, and mask out small gaps and outlier pixels by comparing the smoothed and unsmoothed maps. We compute the raw data counts per pixel \mathbf{D}_{raw} by taking the usable map pixels within each bin shown in Figure 1 and averaging their counts.

We next must estimate the mean, uncertainty, and covariance matrix of the contribution from “background” sources unrelated to the GSS.² To do so, we first select regions in the extreme N and S far from M31 and its substructure, fit a linear model in η (which varies nearly parallel to galactic latitude b in the survey region) to estimate the Milky Way and background galaxy contribution, and subtract this off to eliminate contaminants present across the entire map. This leaves only the contamination from M31's smooth and tidal components.

To estimate this latter source of contamination, we first define a region relatively free of tidal features as follows. We define ellipses aligned with M31's disk following the estimated halo axis ratio of 0.6 (Pritchet & van den Bergh 1994). Marching outwards in elliptical annuli, we mask out pixels in the smoothed map that are 5σ above the mean annulus value, then recalculate the mean and repeat the masking. After also masking any pixels within the test bins shown in Figure 1, we obtain a background estimation region where the GSS, NE and W shelves, and several other tidal features have been masked out.

We assume the M31 “background stars” are roughly symmetric about M31's center. To estimate the mean background value in each bin and the covariance between bins, then, we therefore spin the entire bin pattern around M31 and measure the mean and covariance values averaged over spin angle. Since we are assuming an average axial ratio of 0.6 for the background component, we distort the bins to follow ellipses of this shape. We use 30 evenly spaced orientations, and exclude the masked region from the measurements. For each bin and orientation we measure the counts per usable pixel. Averaging over orientations yields our mean M31 background estimate for each bin. We also measure the dispersion in values from different orientations, which becomes the background uncertainty $\sigma_{bg,i}$, so that the background covariance matrix on the diagonal is $C_{bg,ii} = \sigma_{bg,i}^2$. Estimating the covariance of background estimates in pairs

of bins is more difficult. For each pair of bins we measured the cross-correlation, but most pairs have only a few spin orientations where both bins are in the background test region making this an unreliable estimate. Combining the sample of pairs, we find the median correlation coefficient of neighboring bins (those sharing a common edge) is about 20%. We therefore set the covariance matrix coefficient for neighboring bin pairs to 20% times the measured bin dispersions: $C_{bg,ij} = 0.2\sigma_{bg,i}\sigma_{bg,j}$. We zero out all covariance matrix elements for non-neighboring bins. We compute the total covariance matrix \mathbf{C}_{im} by placing the combined shot noise variance of the observation and simulation terms onto the diagonal, adding a diagonal error term corresponding to 10% variation in the total counts (to generously account for the influence of the artifacts discussed above), and adding these to the background covariance matrix \mathbf{C}_{bg} . Typically the background fluctuations and systematic error terms are the largest error source on the diagonal of \mathbf{C}_{bg} , with the simulation shot noise next and the observed shot noise the smallest.

We then add back the smooth Milky Way and galaxy term to obtain the total background mean \mathbf{D}_{bg} . Finally, we subtract this from the raw bin values to obtain our signal estimate $\mathbf{D}_{im} = \mathbf{D}_{raw} - \mathbf{D}_{bg}$. For the bins with obvious GSS contribution, this signal is $\gtrsim 5\sigma$ above the background level. The raw count values $D_{raw,i}$, background values $D_{bg,i}$, and background uncertainties $\sigma_{bg,i}$ are listed in Table 4. We have investigated alterations to this procedure, including the choice of spherical symmetry for the background calculation and changes in the number of orientations or coverage maps, and generally find quite similar results for the means and dispersions of the background counts in the bins. We thus have some confidence that our background characterization is reasonable.

Next, we must calculate the effective number counts due to the simulation, M_{im} . We calibrate star counts to mass using a theoretical stellar population based on observations of the GSS itself. Our goal is m_1 , the total stellar and stellar remnant mass associated with the detection of one M31 star within our color-magnitude cut. We first convert our INT cut to Johnson V , I with equations in McConnachie et al. (2005). Using the IAC-Star code of Aparicio & Gallart (2004), we then set up a series of 10 Gyr age stellar populations corresponding to the GSS metallicity bins in Figure 27 of Ibata et al. (2007). We normalize each bin population by the height of the bin (since that plot shows relative counts), and also correct for the varying fraction of stars within the magnitude range used in constructing the distribution. We assume a “diet” Salpeter initial mass function (defined as in Bell & de Jong 2001 to have 70% of the mass of the normal Salpeter IMF spanning 0.1–100 M_{\odot}). We then compute the number of counts expected within our color-magnitude cut chosen previously, as well as the stellar mass remaining in the population. Finally, we obtain a mass conversion factor of $m_1 = 1.80 \times 10^4 M_{\odot} \text{count}^{-1}$. Given uncertainties in the population synthesis models, the IMF, and the observed stellar population of the GSS, m_1 is probably uncertain by ~ 0.2 dex or so.

In our likelihood computation, we simply count the particles within each sky bin to get \mathbf{N}_{sim} , multiply this by the mass ratio m_p/m_1 , where m_p is the simulation particle mass, and divide by the number of pixels in each region.

² Our use of the term “background” is not meant to suggest anything about the spatial position of the contaminating sources, most of which indeed are foreground Milky Way stars.

This yields the equivalent model counts per pixel in each bin, \mathbf{M}_{im} . Now we combine all of these quantities to obtain the image likelihood. It is well known that using a χ^2 test in the case of Poisson statistics can lead to biased results. However, in our case the observed count values are large enough that we expect this bias to be minor. In addition, the observational errors are actually dominated by background/foreground fluctuations from unrelated components of M31’s halo, background galaxies, and Milky Way stars, and earlier we estimated this background to have significant correlations between bins. Thus the only practical choice in this case is to use a matrix χ^2 form for the likelihood:

$$L_{im} = -\frac{1}{2}\chi_{im}^2 = -\frac{1}{2}(\mathbf{D}_{im} - \mathbf{M}_{im})\mathbf{C}_{im}^{-1}(\mathbf{D}_{im} - \mathbf{M}_{im}). \quad (2)$$

In an earlier version of our sampling we found a sizable minority population of states with strange-looking W Shelf morphologies, not matching the sharp edge visible in Figure 1. We traced the origin of these states to the large background uncertainties assigned to the W Shelf bins, which in our automated procedure are influenced by structure near M31’s disk. Fortunately, a kinematic survey along the NW minor axis clearly distinguishes between the GSS debris and smooth halo components (Fardal et al. 2012). This paper provides an accurate estimate of the fraction of red M31 RGB stars (those with $[\text{Fe}/\text{H}] > -0.75$, roughly corresponding to our color-magnitude cut) that belong to the GSS shelf: 0.84 ± 0.05 . This allows an independent means of subtracting the background. The spectroscopic survey overlays bins 10 and 12 in Figure 1, though with a much smaller azimuthal coverage, and we take this survey to be representative of these two bins, which we combine into a single minor-axis W Shelf region. Our estimate from the INT survey for the source surface density in this region was 2.81 arcmin^{-2} . Subtracting the estimated Milky Way and background galaxy component of 1.27 arcmin^{-2} , and generously assuming 30% error in this, we estimate the M31 and GSS counts together to be $(1.54 \pm 0.38) \text{ arcmin}^{-2}$. Multiplying this by our estimate of the GSS fraction gives a GSS debris count of $D_W = 1.29 \text{ arcmin}^{-2}$ in this region, with uncertainty $\sigma_W = 0.32 \text{ arcmin}^{-2}$. We augment the likelihood expression in equation 2 with the term $L_W = -(D_W - M_W)^2 / (2\sigma_W^2)$ to constrain the model further.

2.4.2 Stream and lobe position

Our next observable is the estimated sky position of the GSS proper. This ultimately derives from the same photometric survey map as was used to compute the image likelihood. However, we find it useful to treat these two observables separately. The way we have set up our GSS bins, with the broad central bin and the two outer regions added to give a single “outtrigger” bin, ensures the GSS position has only a second-order effect on the surface density term in the likelihood, making it legitimate to include both quantities. The stream position can be estimated without doing an N -body simulation using the stream-orbit approximation of 2.2.1. It can also be estimated where uncertainty in the foreground/background subtraction makes the surface density unreliable, such as the GSS at large radius. Conversely, the density can be measured even in regions where a stream position is ill-defined, as in the W Shelf.

Our starting point is the location of the 8 southern fields F1 through F8 taken with the CFHT12K camera on CFHT in McConnachie et al. (2003), which were centered close to the GSS transverse density peak and were used to obtain the distances used later. We use the slope in ξ and η of these positions to define an M31-centered coordinate system (m, n) , with unit vectors having coordinates in the (ξ, η) system of $\hat{\mathbf{m}} = (0.504, -0.864)$ (along the stream to the SE) and $\hat{\mathbf{n}} = (-0.864, -0.504)$ (across it to the SW). Here we treat m as the independent and n as the dependent variable. We then compare these field locations with the map of “red” RGB stars in the INT survey (Irwin et al. 2005), which is here functionally identical with the map shown in Figure 1. From a histogram of counts as a function of n , we find a peak at about $n = 0.34^\circ$. This also appears consistent with the peak positions in bins centered on the individual fields, so we use this location in each bin as our stream position D_{pos} ; these are offset by about 0.07° to the SW from the field centers in McConnachie et al. (2003). We discard fields F1 and F8, since in both fields it is difficult to estimate a well-defined stream position. The width of the stream obtained using Gaussian+baseline fits is about 0.2° (Font et al. 2006), and we conservatively take this to be the observational error $\sigma_{D, pos}$ on the stream positions. The positions used are shown in Figure 1 and listed in Table 3.

To minimize noise in the likelihood, and avoid contamination from other radial wraps, we use the stream locus estimated from the stream-orbit approximation rather than computing it directly from the simulation. We interpolate the value of n from this locus at the values of m corresponding to the field positions in the table. We tested the performance of this model in some early samples of simulation runs, obtained in the manner discussed in Section 2.6. We estimated the mean position directly from the simulation particles, applying distance and velocity cuts to isolate the stream, and iteratively applying a smooth window function in the transverse direction to find the mean n around each field position. From comparison of these estimates with the stream-orbit estimate we found on average the latter was biased by -0.13° , so we correct the estimate by this amount in our likelihood function. We also found a degree of scatter, which can be represented by a statistical error on each data point of $\sigma_{M, pos} = 0.24^\circ$. We add this theoretical uncertainty in quadrature to the observational error, so that $\sigma_{pos} = (\sigma_{D, pos}^2 + \sigma_{M, pos}^2)^{1/2} = 0.32^\circ$. The position term in the likelihood is then

$$L_{pos} = -\sum_{i=1}^{N_{pos}} \frac{(D_{pos,i} - M_{pos,i})^2}{2\sigma_{pos}^2} \quad (3)$$

Since our scenario asserts the second loop of the orbit (the next one in front of the GSS), lies in the NE Shelf region, we add another likelihood term to encourage this behavior. We base the term on the apocenter position of this orbital loop, which we set to lie in the vicinity of $\xi = 1.8^\circ$, $\eta = 0.65^\circ$; this translates to a projected radius $D_R = 1.9^\circ$ and a position angle of $D_{PA} = 70^\circ$. We assigned loose constraints of $\sigma_R = 1.0^\circ$ and $\sigma_{PA} = 25^\circ$. The corresponding model values are taken from the apocentric position of the NE Shelf in the orbital calculation. The lobe likelihood term

$$L_{lobe} = -\frac{(D_R - M_R)^2}{2\sigma_R^2} - \frac{(D_{PA} - M_{PA})^2}{2\sigma_{PA}^2} \quad (4)$$

helps nudge the parameter states early on in the sampling toward the desired orbital trajectories. Otherwise it is not a particularly strong constraint on our model, and later we check that removing it makes little difference to our most important parameters.

2.4.3 Stream distance

Another likelihood term is based on the distance to the GSS proper, as estimated from the tip of the red giant branch (TRGB) by McConnachie et al. (2003). We use the outermost 7 GSS fields from that paper; the innermost field does not follow the trend of the others, and it is likely to be contaminated by other structures including M31's disk and inner spheroid. The positions of these fields are shown in Figure 1 and listed along with the derived distances D_d in Table 3. We assume a statistical distance error in each field of $\sigma_{D,d} = 20$ kpc as estimated in McConnachie et al. To compare to simulations we assume the distance of M31 is 780 kpc, as estimated using the same TRGB method in McConnachie et al. (2005) and Conn et al. (2012).

These TRGB distances probably also have systematic offsets due to the combination of stellar population uncertainties and the specific algorithm for determining the tip magnitude. We assume these systematic offsets affect each field's distance by the same factor. Equivalently to first order we can substitute a linear *shift* Δ in each field's distance, defined so that the true distances are systematically larger by Δ than the observationally derived values.

We assume a Gaussian prior for Δ described by mean $\bar{\Delta}$ and dispersion σ_{Δ} . Brown et al. (2006) measured the red clump brightnesses within the stream, 21 kpc in projection from the center of M31, and in a minor-axis, spheroid-dominated field. They found the stream was only (11 ± 5) kpc more distant than the spheroid position, which is likely at M31's distance to within a few kpc. Interpolating the distance at their stream field from the measurements of McConnachie et al. (2003) gives 50 kpc. Therefore we assume a best-estimate offset of $\bar{\Delta} = 11 - 50 = -39$ kpc. We take the offset's uncertainty to be $\sigma_{\Delta} = 25$ kpc, reflecting systematic uncertainty in both the TRGB and red clump distance methods.

As with the stream position, we estimate the model's stream distance M_d from the stream-orbit approximation rather than computing it directly from the simulation. This approximation is accurate enough given the large uncertainties in the observed distances, and avoids the contamination from other radial wraps of the GSS that is possible in unusual orientations.

The combination of the distance likelihood and the prior on Δ can now be written as

$$L_d = \sum_{i=1}^{N_d} \frac{(D_{d,i} + \Delta - M_{d,i})^2}{\sigma_d^2} + \frac{(\Delta - \bar{\Delta})^2}{\sigma_{\Delta}^2} \quad (5)$$

Although in principle we could keep Δ as a parameter in our MCMC run, we are only interested in the posterior distribution marginalized over that nuisance parameter. An easier way to calculate this distribution is to solve given each choice of model distance values \mathbf{M}_d for the maximum likelihood value of Δ , which is

$$\hat{\Delta} = \left(\sum_{i=1}^{N_d} \frac{M_{d,i} - D_{d,i}}{\sigma_i^2} + \frac{\bar{\Delta}}{\sigma_{\Delta}^2} \right) \left(\sum_{i=1}^{N_d} \frac{1}{\sigma_d^2} + \frac{1}{\sigma_{\Delta}^2} \right)^{-1}. \quad (6)$$

Using the likelihood value L_d given by inserting $\Delta = \hat{\Delta}$ in Equation 5, one can show this gives the correct posterior distribution of the other parameters marginalized over Δ .

2.4.4 Stream velocity

Our final likelihood term incorporates estimates of the GSS velocity based on six Keck/DEIMOS spectroscopic fields in the GSS core, presented in Ibata et al. (2004) and Gilbert et al. (2009). All the mean velocities are based on fits in the latter paper, which discusses fields a3 (comprising 3 neighboring masks), H13s (2 masks), and f207 (1 mask) in detail. Velocities for fields s1, s2, and s6 (1 mask each) are based on fits to the individual stellar velocity points shown in Ibata et al. (2004). We have assigned a larger blanket uncertainty of 25 km s^{-1} to these three fields, because of concerns that the formal uncertainty is an underestimate in fields with fewer stars such as these, especially in the presence of a clumpy halo component. The data values $D_{v,i}$ and uncertainties $\sigma_{D_{v,i}}$ are listed in Table 3. When comparing to simulations, we assume M31's systemic velocity is -300 km s^{-1} (de Vaucouleurs et al. 1991). We omit fields in the extended envelope to the SW, since from inspection of our previous models (F07, Fardal et al. 2008) we found this can have significant, model-dependent offsets from the core field values. Figure 1 shows the positions of these fields.

The stream velocities are based on small fields where both observations and simulations have small count numbers. To mitigate the effects of simulation noise discussed in Section 2.5.2, we use the stream-orbit approximation to calculate the model stream velocity $M_{v,i}$, as we did already with the stream position and distance. Because the observed velocity uncertainties are relatively small, we measured the offsets between our approximate treatment and the velocity values estimated from the N -body simulations in several early samples of runs obtained with the methods in Section 2.6. We noted systematic trends in the parameters F_p and M_{200} , and used the results from a linear regression in these parameters to apply slight ($\sim 5 \text{ km s}^{-1}$) corrections to the estimated velocities. Typical remaining offsets between estimated and simulated velocities are of order 5 – 10 km s^{-1} , and generally much less than the simulated velocity dispersion in a given field. The worst disagreements come in the outermost fields in cases where the velocity distribution is the furthest from a Gaussian, and characterizing it with a single number is difficult. To be on the safe side we add a rather conservative simulation rms error of $\sigma_{v,M} = 15 \text{ km s}^{-1}$ in quadrature with the observational rms errors: $\sigma_{v,i}^2 = \sigma_{D_{v,i}}^2 + \sigma_{v,M}^2$. The statistical weights assigned to the different fields are thus more equal than initially apparent. We then assume the data points are independent, and calculate the velocity term in the likelihood using a χ^2 form:

$$L_v = - \sum_{i=1}^{N_v} \frac{(D_{v,i} - M_{v,i})^2}{2\sigma_{v,i}^2} \quad (7)$$

We have now enumerated all the terms in the likelihood function. The total likelihood function is obviously

quite complicated, and one may wonder about the sensitivity of the results to the various parts of the likelihood. Our Bayesian treatment enables us to test this formally once we obtain the parameter state samples in the next section. We simply obtain new likelihood values for the states with the altered likelihood function, weight each state by the ratio of new to old likelihoods, and compute new parameter means and dispersions for the sample using these weights in the averaging. Effects we tested include: changing the mean of the distance prior from $\bar{\Delta} = -39$ kpc to $\bar{\Delta} = 0$, altering the position formalism to assume correlated errors, omitting the NE Shelf lobe term, and dropping the model correction terms to the position or velocity. The resulting changes in the means of important parameters such as F_p , M_{200} , and M_{sat} are well below their dispersions, indicating the results are not strongly sensitive to any one of these assumptions.

2.5 Sampling method

By now we have defined several spaces of physical parameters (such as the satellite and halo mass, etc.), and defined both the likelihood and the prior probability on these model spaces. The goal of this project is to sample the posterior distribution—the prior times the likelihood—in parameter space, and thereby obtain the probability distribution of the parameters and any quantity relating to them, including the distribution of quantities obtained directly from the simulated satellite debris. We first discuss the main strategies we use to perform this sampling, and then discuss the impact of simulation noise on our results.

2.5.1 Sampling strategies

We sample the posterior distribution using the Metropolis-Hastings algorithm for Markov Chain Monte Carlo (MCMC) (e.g., Gelman et al. 2003; Press et al. 2007). This uses a series of steps in one or more Markov chains. At each step in the chain, we use a “proposal function” to generate a trial parameter vector, or “state”, from an old one. Depending in part on the new value of the posterior probability compared to the old one, the chain may move to the trial state or remain at the old one (in which case the trial state is discarded). After a sufficient number of steps, which is highly problem-dependent, the chains should reach an equilibrium where it fairly reflects the posterior distribution. We use the Bayesian Inference Engine (BIE), a parallel, scriptable, checkpointing MCMC code written in C++ that implements numerous sampling algorithms (Weinberg 2012a). In the discussion here we assume the posterior distribution has a simple, basically unimodal form, which we will test later for our real problem.

The choice of proposal function in MCMC is important. The step size must avoid the extremes of small steps that fail to go anywhere, as well as large steps that fail to focus on the peak of the sampled distribution. In addition, correlations between parameters can make convergence difficult. The specific MCMC technique we prefer is Differential Evolution MCMC (DE-MCMC, Ter Braak 2006). This is nearly a standard Metropolis-Hastings algorithm, except that the proposal function depends on the population of current states in the different chains. The chief advantage of this technique is that it automatically adapts the widths

and covariances of the proposal function to the shape of the sampled function, obviating the need to set these manually. The method generates a proposed state vector for a given chain by incrementing the current state by the difference of two state vectors from other chains, scaled by a parameter γ . For a normal distribution in a parameter space of dimension d , the optimal scaling parameter is $\gamma = 1.7d^{-1/2}$. Our posterior distributions are not exactly normal distributions, and we find it more effective to set the scaling parameter at a smaller value $\gamma = 1.0d^{-1/2}$. We run with 32 parallel chains, which is enough to ensure reasonable sampling of the state difference vectors for our dimension values. DE-MCMC requires the chains to advance in a synchronized fashion, which motivates a load-balancing scheme. At each step, we crudely estimate the computation time required for each simulation and allocate the pool of processors accordingly, to ensure each chain can advance to the next step in a timely fashion.

The goal of our sampling is just to make the posterior distribution reasonably accurate, as measured for example by the quantiles of the marginal distribution of a given parameter. (See the discussion of the desired precision in MCMC in Press et al. 2007.) We might choose a goal of making the 5% and 95% quantiles accurate to 5% when compared to their difference. For a normal marginal distribution in a parameter x , $x_{95} - x_5 = 3.29$, and asymptotically $\sigma_5 = \sigma_{95} = 2.11N^{-1/2}$, implying one requires $N \approx 160$ independent samples for $\sigma_{95} = 0.05(x_{95} - x_5)$. Thus only about 5 independent samples *per chain* are required to reach this precision for a normal distribution.

To estimate how many independent samples we have, we estimate the “cluster length”, the average number of states per independent sample, as $\Sigma_l \rho(l)$, where $\rho(l)$ is the autocorrelation of one element of the parameter vector (normalized by the variance so that $\rho(0) = 1$) and the sum is taken from negative through positive values. Our cluster length varies with different parameters and runs but is typically ~ 70 – 100 . In comparison, the cluster length at the optimal proposal step size when sampling from a d -dimensional normal distribution is roughly $3d$ (Gelman et al. 2003), which would be no more than 24 for our spaces. The decreased efficiency in our case is due both to deviations from a normal posterior distribution and the presence of outlier chains. When we detect convergence, we typically sample an additional ~ 250 steps or 8,000 states to ensure the distribution is adequately sampled. We define convergence by a combination of the Gelman-Rubin test (see Gelman et al. 2003) and by-eye inspection of the parameter values, likelihoods, and autocorrelation functions of the chains.

Although our focus is on sampling rather than optimization, in the course of developing the model it can be useful to precede the sampling run with an optimization run, to obtain a single canonical model and to check for problems with the likelihood function. We do this simply by making the acceptance step “greedy”, always accepting the higher likelihood state. (This optimization algorithm is known as Differential Evolution or DE, as opposed to the sampling algorithm DE-MCMC.) Selection of an optimal state is intrinsically imprecise in the face of the noise in the likelihood function we discuss later, and this algorithm is not particularly quick to reach convergence. However, it is certainly

preferable in our case to gradient-based fitting methods that assume smoothness.

In some cases, we choose our initial parameter values by sampling uniformly from the prior. However, for poor parameter settings that only put tidal debris far away from the regions sampled in the likelihood, the likelihood noise becomes very large and makes random-walking to a better region difficult. This suggests we should try to initialize the chains to somewhat reasonable values. The “orbital” model uses most of the likelihood terms in the full simulation-based models, though the star-count term is missing, and it is very quick to compute. We extract a set of parameter samples from the “orbital” sample, add random values for the satellite mass parameters to complete the model space, and use these values to initialize the MCMC chains for the “stellar” and “DM” samples. This leads to much quicker convergence for our MCMC runs using N -body simulations.

2.5.2 Effect of noise

Our likelihood function depends in part on an N -body simulation, which stochastically samples phase space with tracer particles. The Poisson noise in the simulation translates to noise in the log-likelihood function and therefore an equal noise in the log-posterior function. (Of course depending on the simulated problem, particle noise can also have *systematic* effects or seed differences in outputs through chaotic dynamics. We believe that our problem is in a simpler regime where Poisson noise is the dominant effect.) For simulations with too few particles, the noise may prevent the the run from converging or render the sampling results inaccurate. On the other hand, if many N -body particles are used in an effort to decrease the particle noise, the computation may slow down to the point where the entire sampling project becomes impractical. Thus it is important to determine whether there is some level of likelihood noise that can offer adequate sampling results. Standard treatments of Bayesian sampling offer little guidance on this issue, though various approaches have been offered in different disciplines (such as Flury & Shephard 2011). We have tried to address it ourselves with a combination of toy analytic models and empirical tests.

Even for a perfect model, a simulation will be offset from the true value by some amount, which will differ from one simulation to the next. Let us consider for now a model in which the observational and simulation rms errors are Gaussian, leading to a likelihood function with the χ^2 form (which is the indeed the form of most terms in our likelihood function). Suppose also the data points are uncorrelated and both the observational rms errors σ_o and simulation errors σ_s have equal values for each data point. To take account of the simulation errors, we must write the log-likelihood as

$$\ln \mathcal{L} = -\frac{1}{2}\chi^2 = -\frac{1}{2} \sum_{i=1}^n \frac{(x_{i,o} - x_{i,s})^2}{\sigma_o^2 + \sigma_s^2}. \quad (8)$$

If the simulation errors were dominant, $\sigma_s \gg \sigma_o$, we would find the well-known result that each data point contributes 2 on average to the variance of χ^2 , or 1/2 on average to the variance of $\ln \mathcal{L}$. In general, averaging over both observational and simulation errors, one can show each point should contribute $2^{-1}\sigma_s^2(\sigma_s^2 + 2\sigma_o^2)(\sigma_s^2 + \sigma_o^2)^{-2}$. For the case

where $\sigma_s = \sigma_o$, this implies a contribution to the variance of $\ln \mathcal{L}$ of 1/6 per bin on average. For typical MCMC calculations, the posterior sampler samples log-likelihood values contained within 10–20 of the peak value. In the regime where $\sigma_s \sim \sigma_o$, one clearly cannot afford too many terms in the likelihood before the likelihood noise swamps the true variation in the likelihood.

What then is the effect of this noise on the parameter sampling? We have explored the effect of likelihood noise using both toy analytic models and simple one-dimensional sampling experiments. We find that likelihood noise does not affect the sampled parameter distribution as long as the noise is constant in parameter space. If instead the likelihood noise varies strongly with parameter values, the estimated distribution can be highly distorted. Another symptom of likelihood noise is that the likelihood values are biased to high values. In fact, the character of the Metropolis-Hastings random walk changes to a series of infrequent jumps from one noise spike to another, slowing the convergence to equilibrium.

One technique we have found useful is occasional resampling: once every N_{rs} steps, we rerun the likelihood computation on the *same* parameter set, but using a new random seed, and use the new likelihood value rather than the old. This dramatically cuts down on the number of states that get stuck on noise spikes, speeding state mixing and convergence. In simple tests with 2- d Gaussian functions, we found a wide range of values of N_{rs} were useful, adding little overhead while greatly improving the mixing. We adopt the value $N_{rs} = 13$ throughout. The drawback of the occasional resampling technique is that it can distort the sampling results. Because the resampled likelihood value is unbiased, likelihood noise enhances the probability of accepting a new, intrinsically inferior state in subsequent states, leading to parameter distributions that are biased high in the tails. For sufficiently small noise levels ($\sigma_L \lesssim 1$), we found this was not a large problem in the test runs.

From these simple tests and our experience with the GSS problem, we suggest these rules of thumb:

- The noise is usually not a major problem if it can be kept as low as $\sigma_L \lesssim 0.25$ –0.5 in the central regions where the likelihood is large. For larger noise values, the sampling will encounter increasing difficulty in converging. While there may well be reasons besides likelihood noise for using large numbers of particles (e.g. to resolve physical effects such as dynamical friction), cutting down the noise beyond this target value will not greatly improve the sampling and can lead to excessive calculation times. Our value of 65,536 particles per simulation was chosen in accordance with this guideline.

- For moderate noise levels, occasional parameter resampling as discussed above is useful to reduce the stickiness of the chains and thereby speed convergence.

- The parameter dependence of the likelihood noise is important. While problem-dependent in nature, the noise will usually increase for parameter settings that lead to poor average likelihood values, especially when the simulations yield small numbers of particles in the observed regions of physical space. This can lead to “stuck” chains that fail to random-walk to better likelihood values, a tendency that is compounded by the nature of the DE-MCMC algorithm. If the number of such chains is small, it should not affect the results. If there are many such chains ($\gtrsim 10$ –20% of the to-

tal), the run may need to be restarted with a larger number of simulation particles to reduce the noise.

- The number of observational constraints should be kept as low as possible, since each constraint adds its own noise. Constraints should be kept only if they add substantial constraining power to the likelihood.

- If a term in the likelihood can be estimated analytically rather than derived from a N -body simulation, it may be worthwhile to do so, depending on how accurate the analytic estimate is and how much likelihood noise is introduced by using the simulation. We made extensive use of this tactic here.

2.6 Parameter samples

We have now assembled all the ingredients for our calculation, and are ready to create a large set of parameter vectors sampled from the posterior distribution using the full probability model.

We first generate a parameter sample for the 7-d “orbital” model. This is based only on the parts of the likelihood that can be calculated directly from the chosen orbit with our semi-analytic technique, and does not involve the progenitor mass. In this calculation, we have also omitted the informative prior on the M31 halo mass M_{200} , and instead used a flat prior. This was done principally to expand the range of halo mass sampled, as we had early indications that the simulation-based sampling would prefer higher mass values than the informative prior. The calculation of the orbital sample is extremely rapid because no simulations are required.

We then run our full simulation sampling technique on the 8-d “stellar” parameter space, generating an N -body simulation for each sample and computing the prior and likelihood functions as described above. This run converges to reasonable values (1.2–1.5 depending on the quantity measured) of the Gelman-Rubin \hat{R} convergence parameter (Gelman et al. 2003) within 1046 steps or 33,472 N -body simulations. The computation took about two weeks using 256 Opteron processors in parallel. We discard an initial burn-in period of 500 steps. Four of the chains remain stuck throughout this run in regions far from the mode, with posterior values far below the maximum. We have culled all chains that never come within 4 of the maximum log-likelihood before computing the parameter statistics. This leaves 20,888 remaining states in 28 chains. Using the cluster length computed as described above, we estimate that each chain contain about 6 independent steps, for about 200 independent states total. The frequency of jumping to a different state is 23%, close to the value of 25% that is optimal for sampling from a Gaussian peak.

Next, we conduct a run with the 9-d “DM” model, which includes the effect of dark matter by the simple expedient of allowing the ratio of luminous to total mass M_{lum}/M_{sat} to vary (implemented by scaling our conversion factor for RGB number to dynamical mass). The run converges sufficiently after 1240 steps, and we discard the first 500 steps and 3 outlier chains leaving a sample of 21,460 states total, or roughly 200 independent states.

As mentioned earlier, we also tried two other parameter spaces with fewer dimensions. In our “reduced” parameter space, the only free orbital parameter is F_p and the remain-

ing orbital parameters are frozen out by fitting the orbital model as a function of F_p . The “density” space adds freedom in choosing the progenitor’s central density. Convergence for these lower-dimensional spaces was significantly easier, as the chains found a good likelihood region more quickly and took far fewer steps per independent state (the cluster lengths were ~ 15). We therefore ran for only 453 and 657 steps respectively.

3 RESULTS

3.1 Parameter distributions and likelihood tests

In Figure 2, we show the distribution of several parameters in the 7-d “orbital” sample. Here the panels on the diagonal show the marginal distribution of each parameter, while the others show the joint distributions of pairs of parameters. It is clear that the orbital sample can place almost no interesting constraints on the progenitor phase or M31’s halo mass. This is because a larger progenitor phase can be traded off against a smaller orbital energy to produce nearly the same GSS properties. (To be fair, the sample does favor larger values of the halo mass, and in this sample we have not included the informative prior on this parameter which favors lower values. Combining the two would yield a posterior distribution similar to the halo mass prior, but shifted by 0.1 dex to higher masses.) The parameter results are also summarized in Table 5.

In Figure 3, we show the parameter distributions for the 8-d “stellar” sample, which are also summarized in Table 5. Clearly, the parameters are now much better constrained than for the orbital sample. In F07 we argued that increasing the orbital phase would decrease the density in the GSS and enhance that in the W Shelf. In test runs where we leave out one or the other of these constraints, we see that this is indeed true. Combining constraints from these two regions thus leads to an startlingly accurate determination of the orbital phase, $F_p = 1.24 \pm 0.06$. This then constrains the spatial pattern so accurately that the satellite’s (purely stellar) mass can also be measured precisely, $\log_{10}(M_{sat}/M_{\odot}) = 9.55 \pm 0.09$. In fact, the dominant uncertainties are probably systematic, for example error in the mass normalization constant m_1 calculated earlier. The halo mass M_{200} is the lone parameter to take on a large range of values compared to our initial prior range, $\log_{10}(M_{200}/M_{\odot}) = 12.32 \pm 0.09$, but even it is significantly altered relative to our prior distribution, as seen in the inset. Halo masses as low as our initial expectations are incapable of generating the required GSS velocities, for our well-constrained satellite mass and orbital phase. We will discuss this result in more detail in Section 4.3. The figure also shows a significant correlation between M_{200} and the progenitor satellite’s mass.

We create a “library” of nearly independent simulations of this model by rerunning one state every 100 steps for the converged part of each chain. This yields 6 steps \times 28 chains = 168 states, counting only those in the retained chains. The majority of these states share a morphology similar to that in the observed map in Figure 1, although there are a few unusual-looking states at low likelihood values. We select a sample for display by defining a grid in F_p and M_{200} and selecting representative states near each grid point (see

Table 5. Parameter results

Parameter	“Orbital” sample				“Stellar” sample				“DM” sample			
	Mean	Sigma	95% range		Mean	Sigma	95% range		Mean	Sigma	95% range	
X	0.8564	1.911	-3.308	3.764	1.51	1.17	-0.77	3.84	0.90	1.12	-1.03	3.49
Z	16.33	5.596	7.001	28.72	19.73	2.716	13.66	24.47	18.33	3.234	10.08	24.25
V_x	-94.76	18.05	-133.2	-62.33	-83.9	11.2	-108.9	-64.9	-87.7	13.3	-118.6	-65.6
V_y	183.9	33.94	124.6	255.2	173.7	22.36	137.7	226.0	177.5	25.58	136.1	240.1
V_z	-236.2	30.60	-293.5	-178.4	-244.0	11.24	-263.8	-218.9	-247.6	16.9	-277.1	-207.8
F_p	1.416	0.3270	0.8498	1.966	1.241	0.062	1.112	1.388	1.26	0.16	0.96	1.71
$\log_{10}(M_{200}/M_{\odot})$	12.32	0.1458	11.97	12.50	12.26	0.084	12.10	12.42	12.27	0.10	12.07	12.48
$\log_{10}(M_{sat}/M_{\odot})$	NA	NA	NA	NA	9.550	0.088	9.398	9.742	9.87	0.31	9.22	10.39
$\log_{10}(M_{lum}/M_{sat})$	NA	NA	NA	NA	NA	NA	NA	NA	-0.28	0.28	-0.71	0.35

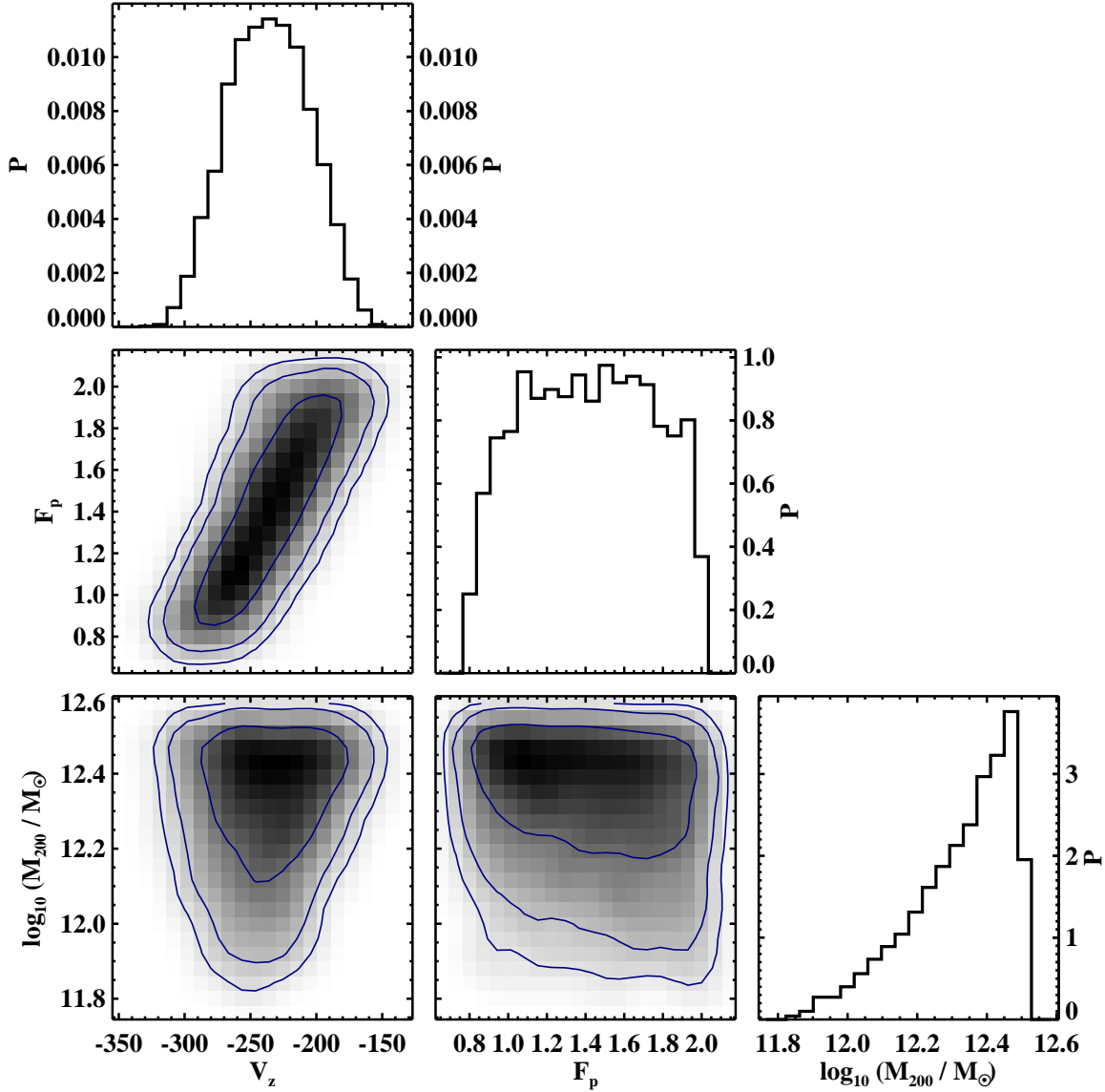


Figure 2. Parameter distributions in the orbital sample. Diagonal panels show the marginalized distributions of individual parameters, while off-diagonal panels show the joint distribution of pairs of parameters. The parameters shown here are the Z velocity at the orbital reference point, the progenitor phase F_p , and the M31 virial mass M_{200} . The phase F_p is calculated using the progenitor’s original orbital trajectory, whether or not it survives to the present time. In this sample a flat prior for M_{200} is used rather than the informative prior (see discussion in the text). Contours enclose 67%, 95%, and 99% of the probability.

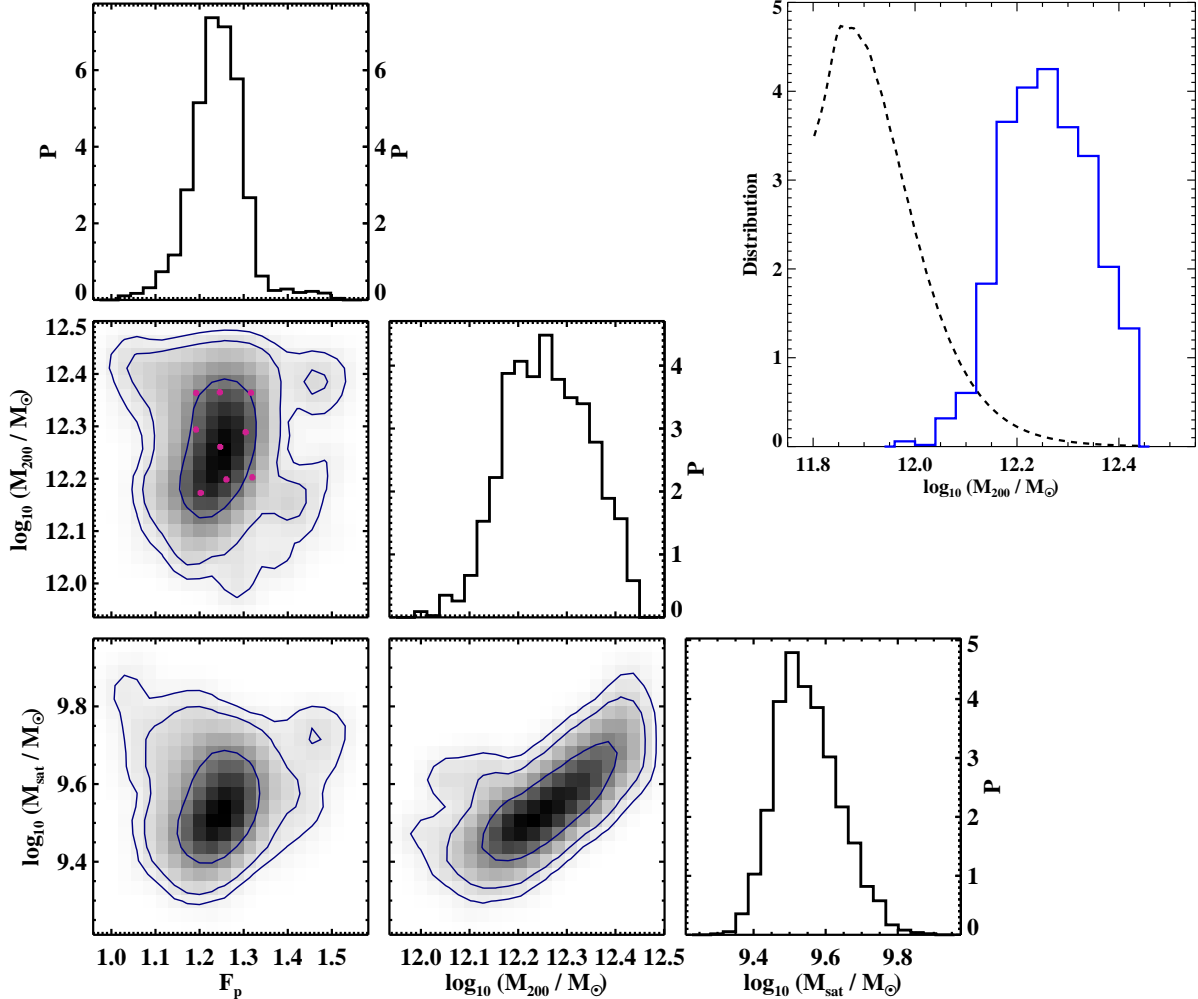


Figure 3. Parameter distributions in the “stellar” simulation sample. Diagonal panels show the distributions of individual parameters, while off-diagonal panels show the joint distribution of pairs of parameters. The parameters shown here are the progenitor phase F_p , the M31 virial mass M_{200} , and the GSS progenitor mass M_{sat} . Crosses in the F_p - M_{200} panel show the rough grid of states to be used in Figure 4. Upper right panel: final distribution of the halo mass (histogram) over the entire prior range, with prior (dashed) also shown.

Figure 3 for their actual locations). Figure 4 displays the sky pattern of these states. Each of the runs shows well-defined GSS, NE Shelf, and W Shelf features. The good agreement of the models with the observed W Shelf edge is achieved by use of the surface density constraints in the W Shelf region (Figure 1). The states here also agree well with the NE Shelf edge, though the variation in this shelf location is larger in the total sample. Some systematic variation of the morphology with the parameter values is apparent: as F_p increases from left to right, so do the W Shelf surface density and areal coverage. Also, as M_{200} increases from bottom to top, the GSS appears shorter and broader. This suggests the correlation between M_{200} and M_{sat} arises because a larger halo mass speeds the return of the GSS material, thus advancing it in phase, which then requires a larger mass satellite to produce a GSS density consistent with observations. However, there are also variations not simply explained by these two variables, including large differences in how much of a central core or clump survives in the NE Shelf region.

In each of these resimulations we calculate the orbital

trajectory of the progenitor assuming a test-particle orbit. In this sample the progenitor has apocenter 55.5 ± 4.5 kpc, pericenter 2.86 ± 0.81 kpc, orbital period 610 ± 60 Myr, and it reached the disruptive pericenter 760 ± 50 Myr ago. A few orbital quantities show strong correlations with particular input parameters. As expected, the apocenter and orbital period are very well correlated and both anticorrelate strongly with F_p . Also, the pericenter is positively correlated with M_{200} . Mostly, however, the dispersion results from combinations of the “uninteresting” orbital parameters. In any case the results show very little dispersion in each quantity, showing that the model predicts a very definite trajectory and history of interaction with M31.

The results of the 9-d “DM” sample are shown in Figure 5 and again summarized in Table 5. The uncertainty on the orbital phase more than doubles, $F_p = 1.26 \pm 0.16$, and that on the progenitor mass more than triples, $\log_{10}(M_{sat}/M_{\odot}) = 9.87 \pm 0.31$. However, the amount of luminous matter and its uncertainty are almost the same as before: $\log_{10}(M_{lum}/M_{\odot}) = 9.58 \pm 0.09$. M_{lum} correlates

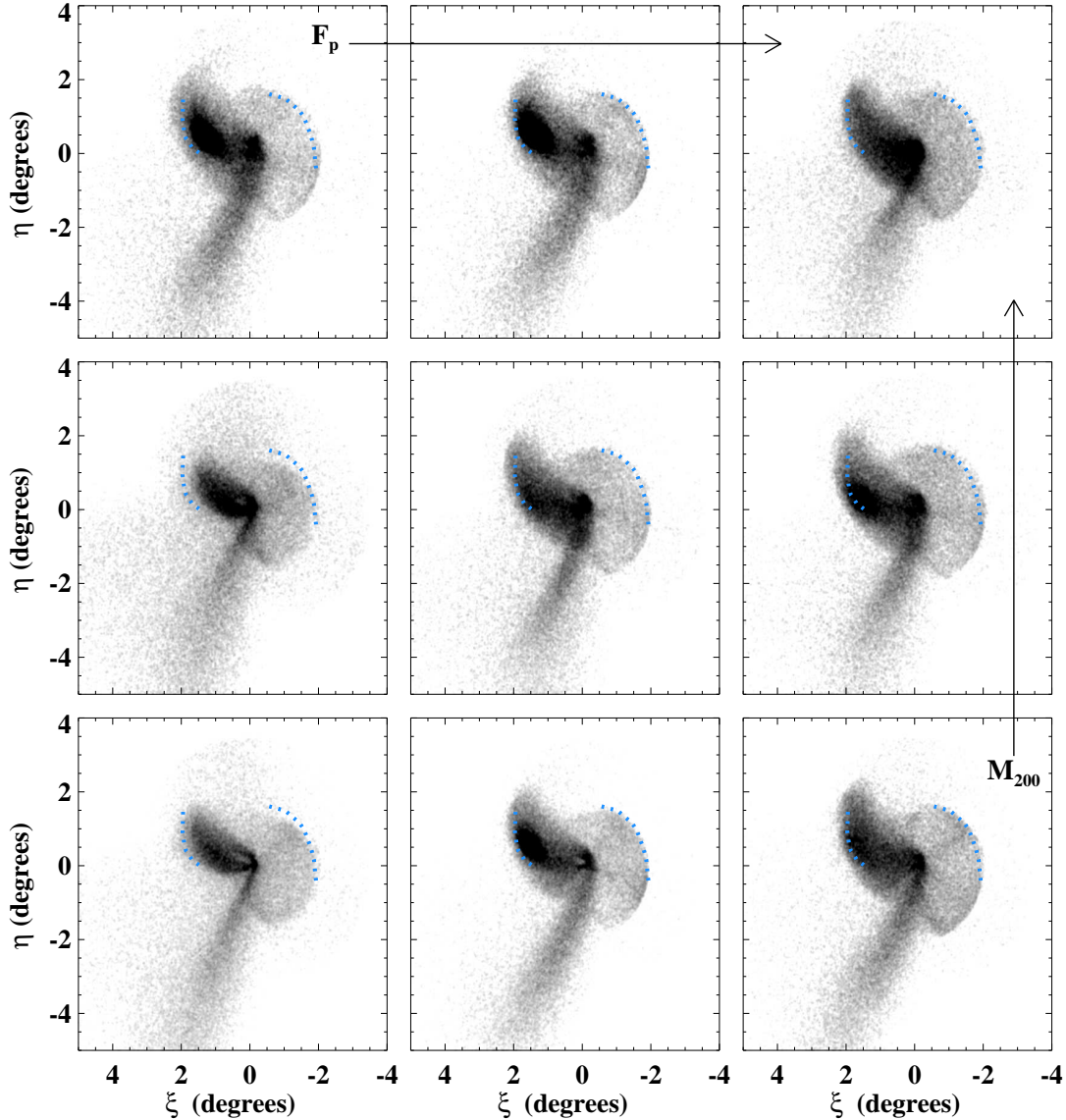


Figure 4. Sky distribution for nine parameter states taken from the “stellar” sample, on a square-root intensity scale. The values of F_p and M_{200} for these states are arranged roughly in a grid around the distribution mean, with separation of about 1σ (see Table 5). F_p increases to the right and M_{200} increases upwards in this grid of plots. Dashed lines show the locations of NE and W shelves from Fardal et al. (2007).

with M_{sat} , roughly as $M_{lum} \propto M_{sat}^{1/4}$. Thus the amount of dark matter is highly uncertain, but the median model contains nearly equal masses of dark matter and stars. The halo mass and its uncertainty are barely affected by the change in model.

We again create a library of nearly independent simulations by rerunning one state every 100 steps for the converged part of each “DM” chain, yielding $8 \times 29 = 232$ states. Inspection of this sample helps us interpret the correlation of M_{lum} with M_{sat} : higher values of M_{sat} spread out the tidal debris over a larger region, requiring a larger M_{lum} to keep the surface densities at observed levels. The variety in this simulation library is enhanced relative to the “stellar”

sample, but as before most simulations share the same basic morphology.

Most of the observational constraints are very well satisfied in both of our models. As an example we display the GSS distance and velocity for one of the “stellar” model states in Figure 6. The observed gradients along the stream—infalling from behind M31, and speeding up along the way—are very well reproduced in our model.

The maximum likelihood value in the “stellar” sample is -9.4 , corresponding to an effective χ^2 value of 18.9 for 28 degrees of freedom (6 stream positions, 7 stream distances, 6 stream velocities, 2 NE lobe positions, 1 galaxy potential prior, and 14 surface density regions, minus 8 parameters), which is quite reasonable. (Simulation noise should bias the

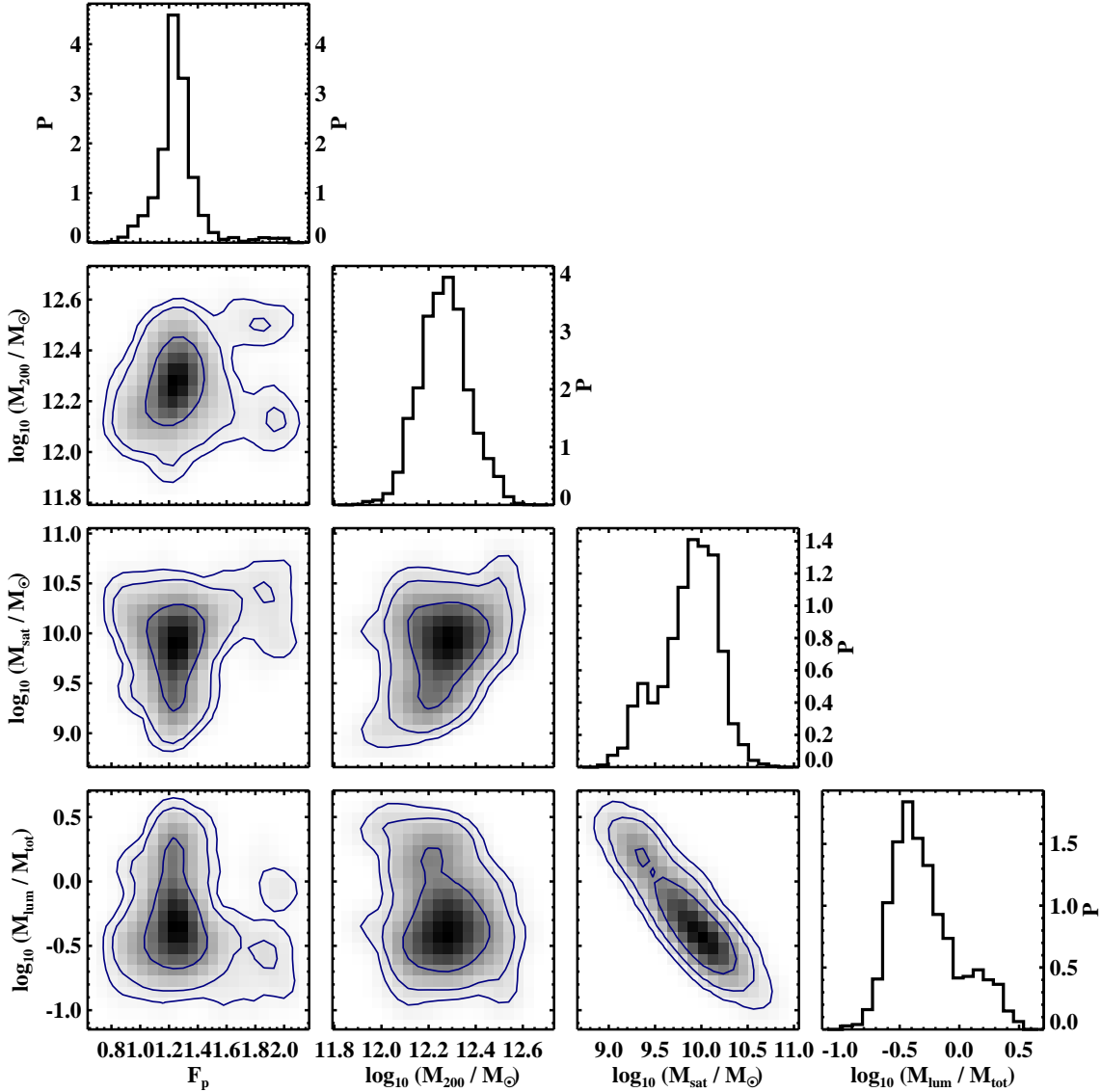


Figure 5. Parameter distributions in the “DM” simulation sample. Diagonal panels show the distributions of individual parameters, while off-diagonal panels show the joint distribution of pairs of parameters. The parameters shown here are the progenitor phase F_p , the M31 virial mass M_{200} , the GSS progenitor mass M_{sat} , and the GSS luminous to total mass ratio M_{lum}/M_{tot} .

maximum likelihood value upwards. Estimating this effect with a mean noise of $\sigma_{LF} = 0.5$ and 8 degrees of freedom suggests the 99.8% quantile of the resimulated distribution is a good estimate of the true maximum LF value, and we have in fact defined our maximum likelihood value this way. We have also incorporated the galaxy prior value into this estimate of χ^2 , via a term $-2(\ln[P(M_h)] - \max\{\ln[P(M_h)]\})$, since it is variable whereas all other parameters have uniform priors.) If anything, the fit is unexpectedly good, with a probability of a better one by chance of only 10%. Though it is possible we have underestimated the positive bias of simulation noise on the maximum χ^2 , we ascribe the low χ^2 value primarily to some combination of luck and possible overestimation of the observational errors. The maximum likelihood value in the “DM” model is -9.0 , corresponding

to an improvement in χ^2 of only 0.8 achieved with 1 extra parameter, which indicates no superiority of this model.

Besides the halo mass parameter, the only datapoint that is consistently more than 1σ off is an outer W shelf region; this region’s background-subtracted surface density is negative, which the simulations naturally cannot reproduce. A common though mild deficiency of the models is in the GSS region, where the models find it difficult to achieve a density gradient along the stream as large as in the observations. It remains to be seen how much of this discrepancy is due to unsubtracted variations in the background, and how much reveals true deficiencies in the model. The density distribution within the satellite may play a role, perhaps motivating a more complex model than the Plummer sphere employed here. The models also may introduce more curva-

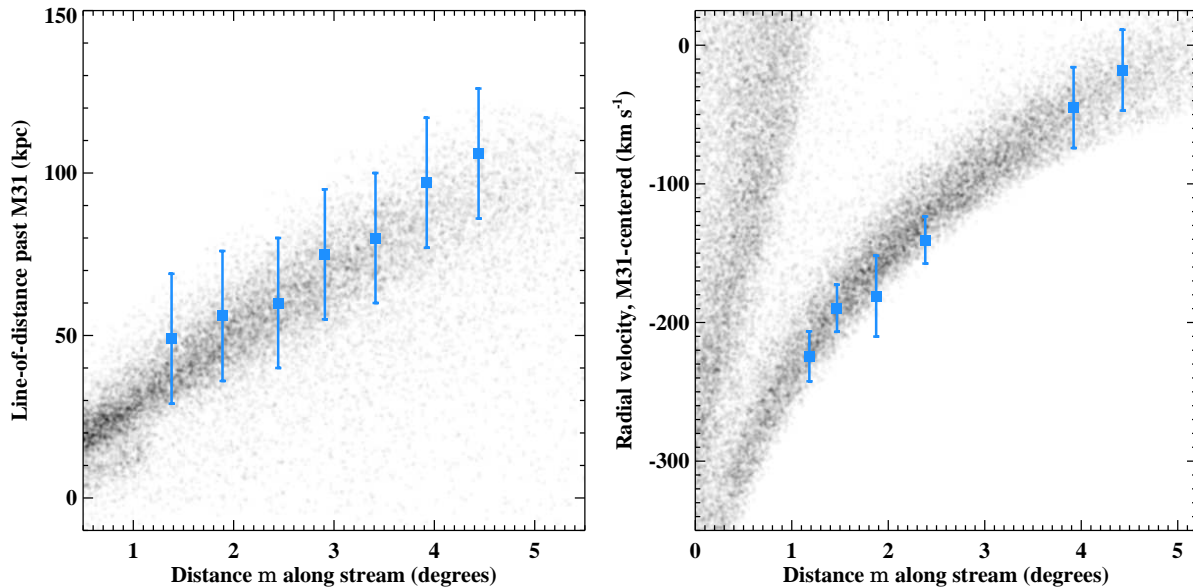


Figure 6. GSS properties of the central panel in Figure 4. Left panel: distance to points along GSS, as a function of pathlength along the stream, compared to data in McConnachie et al. (2003). We apply cuts in stream transverse position $1 < n < 3$ and in M31-centered velocity $v_{M31} < 30$ to select predominantly true GSS particles. The m - n coordinate system is depicted in Figure 1. Right panel: mean velocity at points along GSS, compared to data in Gilbert et al. (2009). The triangular feature above the GSS in the simulation is mostly NE Shelf material on the near side of M31.

ture into the stream velocity than suggested by the observations (as seen in Figure 6), though usually only a single data point (at 2.3°) is visibly offset. The scatter between different resimulated models is comparable to the size of the observational error bars.

We can test whether either of our models is preferred by means of the Bayes ratio, which is the ratio of the integrated likelihood or “Bayesian evidence” in each model. General use of the integrated likelihood would require us to take more care in specifying our prior. But in our case, where the models are “nested” and one simply incorporates an additional parameter, the uncertainties in specifying the prior mostly cancel out in the Bayes ratio. The integrated likelihood is not straightforward to compute from a MCMC parameter space sample, and the “harmonic mean” formula sometimes recommended for this purpose yields spectacularly poor results here. We calculate the integrated likelihood by means of the volume tessellation method of Weinberg (2012b). The maximum log-likelihood is only 0.25 larger in the “DM” than in the “stellar” model, and this is canceled out by the smaller fraction of parameter space occupied, giving a final Bayes ratio close to unity. Another way to compare the models is the value of $-2 \ln L = \chi^2$ averaged over the parameter sample (Johnson 2005). This is again very close in the two models. Therefore, a modest dark matter contribution in the progenitor is quite plausible, though not in any way preferred by the data, whereas a cosmological baryon to dark matter ratio is ruled out.

We note that the use of an informative prior on M_{200} is important in obtaining its nicely peaked distribution visible in Figures 3 and 5. Specifically, the prior factor from Gehan et al. (2006), based on kinematic observations of M31 and its halo tracers, is peaked around $M_{200} = 12.0$ and acts to pull down the distribution on the high side (see

the separate panel in Figure 3). Without this factor the peak would probably be raised by ~ 0.2 dex. The likelihood function from fitting the GSS, in contrast, prefers higher masses and pulls down the low side. The other factors in our halo prior are less important and can be significantly altered without much effect on the results. Thus any follow-on from this study should probably begin by reassessing the prior from M31’s kinematic tracers. In contrast, the other priors used in this work are mostly not very significant. For example, multiplying the flat prior on $\log_{10} M_{sat}$ in the “stellar” model by M_{sat}^{-1} shifts the distribution by less than 0.02 dex, and the same is true for $\log_{10} M_{stellar}$ in the “DM” model. The choice of prior gives a larger offset for M_{sat} in the DM model, simply because this parameter is not very well constrained.

We mostly used the “reduced” parameter sample as a preliminary step towards the larger spaces investigated earlier. We also used this sample to compare to the “density” sample, where the characteristic satellite density ρ_{sat} is allowed to vary. The resulting parameter sample shows essentially the same results for F_p , M_{200} , and M_{sat} as for the “reduced” sample. This indicates the satellite density has little effect on the model for most of the parameter range. However, there is a tail to high values of M_{sat} and ρ_{sat} . Inspecting simulations with these values, we find they share a large intact core that retains much of the original mass, thus requiring a larger mass to populate the GSS and W Shelf regions with debris. These runs look to be inconsistent with the lack of an obvious progenitor in the NE shelf region, and we expect that this tail could be ruled out by detailed observations in that region.

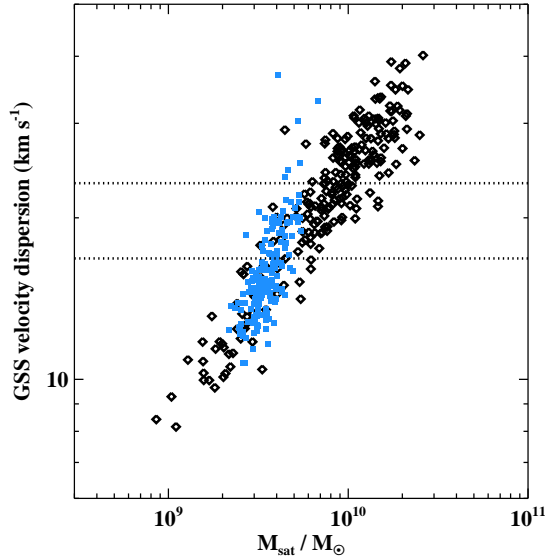


Figure 7. GSS velocity dispersion for the resimulated states in the “stellar” sample, plotted as a function of progenitor mass M_{sat} . Open diamonds show the “DM” sample, and small filled squares show the “stellar” sample. The calculation of the dispersion is discussed in the text. Dashed lines show the minimum and maximum estimated values for the dispersion in the three on-stream fields from Gilbert et al. (2009).

3.2 Model testing and predictions

Beside the reasonable fit obtained by our parameter samples, is there other evidence to believe in our general scenario? We can look for this in a variety of quantities that were not included in the likelihood function, because they were difficult to measure robustly or because of concerns over contamination from other structures in M31. We can also offer some predictions for quantities that have not yet been observed.

One piece of evidence is the generally good agreement of our model states with the observed morphology of red RGB stars around M31 (compare Figures 1 and 4). Recall that only selected regions of this map were used in the fitting procedure, although we also included a term loosely constraining the NE Shelf lobe. In a randomly selected collision model it would be quite easy to produce jets or clouds of metal-rich debris in various directions which are inconsistent with observations; these unwanted features are generally avoided in our simulated states.

We omitted the velocity dispersion in the GSS from our likelihood function for several reasons. First, the dispersion is not entirely straightforward to measure, either in the simulations or observations; in some cases the GSS velocities can have a distribution that is far from Gaussian (often asymmetric to the positive-velocity side), and details of model fitting can affect the results. Also, we have assumed a hot, spherical progenitor; while prior experience with colder progenitors (Fardal et al. 2008) has not shown dramatic effects on the velocity dispersion, in principle a cold progenitor can reduce the dispersion. It is nevertheless worth comparing the dispersion to the observations. For each state in the “DM” sample, we estimate the velocity dis-

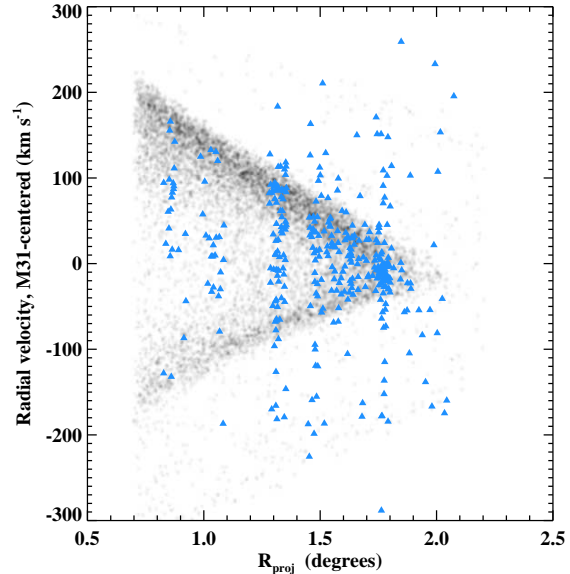


Figure 8. Velocity as a function of projected radius, for stars on the NW minor axis of M31. Here we average together all nine states in Figure 4 to produce the grayscale map, as they are all reasonably similar. Simulation particles are selected in the range $|X_{M31}| < 0.3^\circ$, $0.7^\circ < Y_{M31} < 2.2^\circ$, where X_{M31} and Y_{M31} increase along M31’s SW major and NE minor axes respectively. Triangles indicate the stars classified as M31 giants in the sample of Fardal et al. (2012); these observed stars include not only shelf material but any other components at this position.

person around each of the fields f207, H13s, and a3, which are assigned velocity dispersions of $23.2^{+7.2}_{-5.0}$, $21.3^{+4.0}_{-3.2}$, and $16.8^{+4.6}_{-3.3}$ km s^{-1} in Gilbert et al. (2009). For each field center we first estimate the median velocity, weight each particle with a window function, then estimate the mean, recompute the weight, and re-estimate the mean. (We used a window with a flat top of width 80 km s^{-1} and a rounded falloff of 40 km s^{-1} on each side to gradually downweight outliers from the stream, but the window shape is not very important.) We use the mean of the three field center measurements as our velocity dispersion measurement for each resimulated state. As seen in Figure 7, this turns out to be a function of M_{sat} with a small scatter for most states.

The observed range of velocity dispersion estimates from Gilbert et al. (2009) is shown by the dotted lines. This suggests that both the extreme high and low values of M_{sat} in our DM sample are unrealistic, with the caveats noted before, whereas values of $3\text{--}10 \times 10^9 M_\odot$ are favored. We can formalize this sense through a posterior predictive check (Gelman et al. 2003), where we draw samples from the model velocity dispersions and fold in the observational errors to generate mock replicants of the data. The observed average data velocity dispersion of 20 km s^{-1} lies at the 78% quantile of the replicants using the “stellar” sample, and the 39% quantile using the “DM” sample. Neither value is particularly extreme, which bolsters the sense that our model is reasonable.

We made no explicit use of the W Shelf kinematics in fitting the observed data. Fardal et al. (2012) found the velocities along the NW minor axis, when plotted as a function of radius, could be well described as a mixture of a

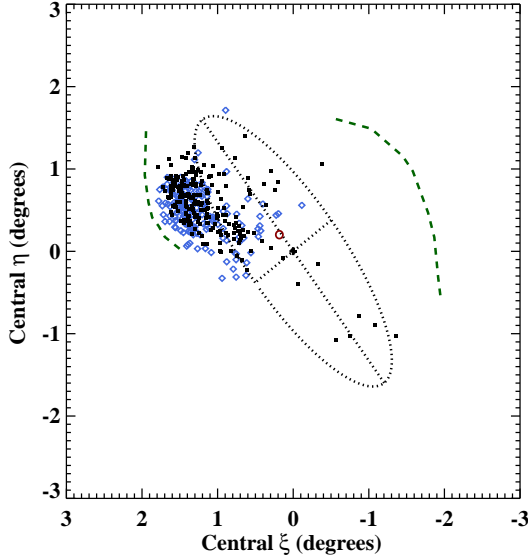


Figure 9. Location of the progenitor’s central material on the sky at the present day. The sample uses the resimulated states for the “stellar” sample (diamonds) and “DM” sample (squares). The definition of the central location is discussed in the text. Annotations are the same as Figure 4. The circle near M31’s center shows the location of the overdensity found by Davidge (2012).

hot spheroid and the wedge pattern expected from a radial shell (Merrifield & Kuijken 1998). Inspecting the kinematics in this region for the states shown in Figure 4, we find no major differences, so we show these combined into one distribution in Figure 8, together with the observed M31 stars from Fardal et al. (2012). (See that paper for further details of the observational sample.) The agreement of the simulations with regions of enhanced density is remarkable. Inspecting our entire sample of states, we do find some variation in aspects such as the radius of the wedge and the contrast between wedge edges and interior. However, the overall morphology is quite robust, again bolstering our model.

Gilbert et al. (2007) found a wedge-like cold feature on the SE minor axis of M31 terminating at a projected distance of about $R_{proj} = 1.3^\circ$, and suggested this was the fourth wrap of the GSS predicted by F07. In the states resampled from both “stellar” and “DM” models, it is quite common to find such a feature, but its strength and definition are highly variable. Often it is completely absent, either because the shell itself is absent or because it does not overlap the SE minor axis. The shell tends to be stronger for larger M_{sat} , so the occurrence of a “SE shelf” feature is more common in the “DM” model. In general the shell extends in an arc around much of M31, which suggests future observations might detect such a feature at $R_{proj} = 1.3^\circ$ at different locations. While the shell is clearly sensitive to the input parameters, indicating it might be a strong constraint on models, we also suspect its properties would be strongly influenced by rotation of the progenitor or a tri-axial potential. Measurement of the shelf surface density in the Gilbert et al. (2007) sample would also be required to make a quantitative comparison with the simulations. Thus at this point neither observations nor models are at a stage

where we can use this feature to constrain the models, but it might become very useful in future work.

For our ensemble of model states, where is the debris from the central core of the satellite located, and should it be clearly evident? The actual state of this central debris can vary from tightly bound to highly dispersed, as can be seen in Figure 4. We determine the location of this debris by selecting the 100 lowest-energy particles in the initial progenitor for each resimulated state, then measuring their mean present-day sky position. The results are shown in Figure 9. Except for a few outliers, which generally have quite low likelihood values, the central debris lies in the NE Shelf region, in many cases projected directly against the disk. The low surface densities relative to M31’s disk may make it difficult to determine the core location from imaging alone. The core debris velocity can take on a large range of values, $-49 \pm 67 \text{ km s}^{-1}$ in our “stellar” sample, so while this is usually distinct from M31 disk velocities (which are $\sim 80 \pm 40 \text{ km s}^{-1}$ in these core positions) it cannot be relied on to uniquely identify the GSS core. It is worth noting that none of our central cores, or even central orbits, pass near M32 or NGC 205 when considered in position and radial velocity space.

Recently Davidge (2012) image-processed 2MASS data to discover an overdensity in M31’s disk, at about 3.5 kpc from M31’s center. He found a magnitude $M_K = 6.5$ (corresponding to a stellar mass of $\sim 3 \times 10^8 M_\odot$) and a size of about 1 kpc, and a composition rich in AGB stars. The size and mass of this overdensity make it a plausible candidate for the GSS core. By comparison to Figure 9, it can be seen that the Davidge overdensity lies at the small-radius edge of the progenitor locations in our sample of states. The nearby progenitor cores in this sample are outgoing rather than infalling, with M31-centered line-of-sight velocities varying from -300 km s^{-1} to -100 km s^{-1} depending mostly on their orbital phase. The disk on this side has positive velocity relative to M31 center, so spectroscopy of stars in this region could yield a diagnosis of this object’s nature. Another possibility *not* covered by our model is that dynamical friction has slowed the core down substantially and caused it to fall in much faster than the rest of the NE Shelf material, so that it would be infalling again at the present time. The sheer amount of material liberated from the GSS suggests that dynamical friction is unlikely to be so effective at the last pericentric passage, due to the progenitor’s lower mass, and we regard this scenario as unlikely.

Detailed inspection of the NE Shelf kinematic tracers will probably be necessary to isolate whatever remains of the GSS progenitor core. In Figure 10, we show the velocity versus projected radius of simulation particles in the NE Shelf region, for the same states as in Figure 4. All states display an overall “wedge” morphology, usually with a strong concentration at the lower boundary which is formed by a caustic in velocity space. As previously seen in F07, this caustic appears to match the planetary nebula “stream” detected by Merrett et al. (2006). This caustic was not fitted to the planetary nebula data, but rather forms naturally as a product of the debris geometry and gravitational potential in our simulations.

While the general pattern of the NE Shelf kinematics is similar in all models displayed in Figure 10, there are also significant variations. Some models have strong concen-

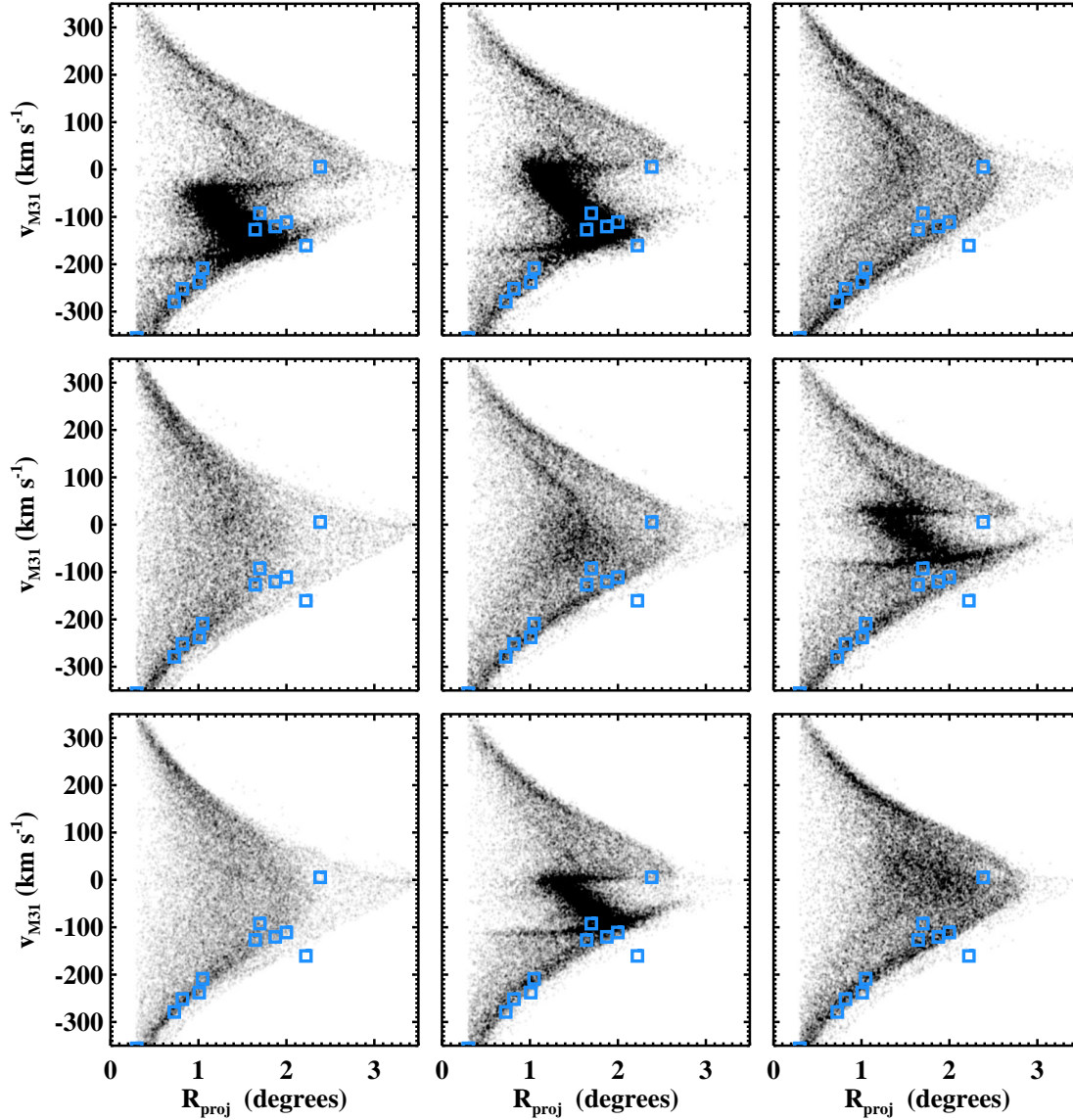


Figure 10. Velocity as a function of projected radius, for stars in the NE Shelf region on and beyond M31’s NE side. The plots show the same nine states as in Figure 4. Particles for this plot are selected in the region $X_{M31} < -0.2^\circ$ and $|Y_{M31}| < 1.5^\circ$, where X_{M31} and Y_{M31} run along M31’s SW major and NE minor axes respectively. The squares show the planetary nebulae labeled as “Stream” or “Stream?” from the NE Shelf region in the sample of Merrett et al. (2006).

trations at the wedge boundaries, while other spread their stars more evenly throughout the wedge. In most models the wedge shape is warped from a pure triangular shape, as a result of second-order effects discussed in regard to the W Shelf region in Fardal et al. (2012). In addition to the lower caustic many models show an upper one, which has not yet been detected. The most striking effects result from the presence of an intact core at the last pericentric passage, resulting in a characteristic zigzag-shaped clump in these plots. Finally, some models show the presence of other radial shells, resulting in a second wedge visible within the main one. Clearly it is difficult to make too definite predictions about the NE Shelf kinematics, but by the same token

these measurements could be quite useful in constraining the GSS model and locating the core debris.

In summary, the models agree well with several observables that were not explicitly part of the fitting process: the sky distribution of metal-rich RGB stars outside the fitting regions, the kinematics in the W and NE Shelf regions, and the velocity dispersion in the GSS itself. The latter quantity is only satisfied for total progenitor masses in the middle of our current distributions, pointing to a possible further constraint on the model, with caveats noted earlier. The model also makes some fairly robust predictions. The debris from the core of the satellite should be located in the NE shelf region, most likely somewhere in a circle of radius 0.6° , and with velocities more negative than expected for the disk

in the same location. The NE Shelf should feature stars at positive as well as negative velocities, possibly including a caustic mirroring the one tentatively detected at negative velocities. Finally, there are features that are highly variable, including the total mass and areal extent of the shell with radius 1.3° corresponding to the fourth orbital wrap, the detailed kinematic pattern in the NE Shelf region, and the velocity and concentration of the core debris. These variable features may be the key to reducing the allowed parameter space and allowing yet tighter constraints on M31's halo mass.

4 DISCUSSION

4.1 Bayesian Simulation Sampling

The results in the previous section show the power of a Bayesian formalism combined with N -body models to constrain physical parameters in a complex dynamical situation. We refer to this as Bayesian simulation sampling. To our knowledge, this paper represents the first application of this technique to models of merging galaxies. The generic concept of using simulations in a Bayesian likelihood evaluation has however been applied in other disciplines (e.g., Flury & Shephard 2011). Our results show it is possible to obtain well-specified parameter estimates, uncertainties, and covariances for merger models, even in cases where simulations are necessary to estimate the observables. This demonstration itself may be more important than the problem-specific results presented here.

Previous sections commented on some pitfalls of the Bayesian simulation sampling method. The main ones are the large computer time required, and biases and convergence difficulties stemming from the stochastic nature in the simulation. We have already discussed some of the techniques used to speed up the calculation, including:

- use of DE-MCMC to automatically choose the shape and scale of the proposal function;
- resampling of the likelihood values, to reduce the effects of noise in the likelihood;
- assignment of reasonable initial chain values based on simpler orbit calculations, instead of randomly sampling from the prior;
- use of a load-balancing scheme which assigns different numbers of processors to different likelihood evaluations, depending on their computational difficulty.

We anticipate there are numerous other ways in which our method could be improved. These might include:

- treatment of likelihood noise through averaging or smoothing. When we sample the same point in parameter space we might be better off averaging the values obtained for that point, rather than simply replacing the value as we have done. It might also be possible to smooth the likelihood over neighboring samples of parameter space (see the model emulation technique of Bower et al. 2010).
- Some directions in parameter space are much easier to explore than others. For example, the parameter M_{lum}/M_{sat} that controls the mass-to-light ratio is trivial to change and does not require a new N -body calculation. Also, the potential is exactly symmetric about the galactic z axis and

is roughly symmetric about the other axes, given our assumed spherical halo potential. We could alternate Gibbs sampling along these “special” directions with Metropolis-Hastings sampling along “generic” directions (Gelman et al. 2003).

- Breaking our likelihood function into an easy part (based on the orbital calculation) and a hard part (based on a simulation). The sampling can then be broken into one Metropolis-Hastings step based on the easy part, and one performed only afterwards on the hard part. Rejected steps in the easy part would free up processors that can be assigned to calculations in the hard part using our load-balancing scheme.

Depending on the problem, we expect the combined effect of these techniques could speed up convergence by a significant factor.

Of course, if the structure of a stream can be described adequately by analytical methods instead of N -body simulations (which is not the case here), a Bayesian approach becomes much easier. Many papers on tidal streams simply assume the central path of the stream follows the orbit of the progenitor. Correctly relating the orbit of a progenitor to the central locus of a stream is an ongoing research problem, and several approximations besides that employed here have been proposed (Johnston 1998; Varghese et al. 2011; Eyre & Binney 2011). Which approximation is best in a given case may depend on the orbit of the progenitor, its degree of intactness, and the observables at hand. Bayesian analyses of tidal streams using any of these assumptions include those of Koposov et al. (2010) and Varghese et al. (2011).

Our own problem was made easy in certain respects by the reasonably simple structure of our posterior function, which had a single dominant mode. Other attempts to fit mergers or tidal substructure with simulation sampling may lead to much more complicated likelihood and posterior functions, especially when fewer types of observational data are available or when the oscillatory behavior typical of dynamical problems leads to multiple modes. In many such cases, the problem may be unfeasible given the large investment of computer time required by the Bayesian simulation sampling technique. In other cases, one may be able to isolate several well-separated modes representing alternative scenarios, impose artificial constraints on the model restricting it to a particular mode, then apply simulation sampling to explore the structure and implications of the domain around each mode. It may be argued that our particular assumptions about the nature of the observed “shelf” morphology and direction of motion of the GSS progenitor are restrictions of this kind. As demonstrated in Section 3.2, an advantage of Bayesian simulation sampling is the easy production of large simulation libraries with parameters sampled according to the posterior distribution. These enable clear observational predictions which can help confirm or rule out the choice of a particular mode.

4.2 The GSS Model

The model for the GSS structure here is that of a satellite disrupted essentially in a single pass, resulting in the trailing GSS as well as a number of other orbital wraps. While the

basic model cannot yet be considered proven, it does pass a number of observational tests, based on both morphological and kinematic data. Our model implies that the GSS is due to a previously unknown satellite of M31, not any of the currently intact ones such as M32 or NGC 205.

The general pattern of the individual simulations is similar to that found in earlier work. The simulation used in Fardal et al. (2012) is one fairly representative element of our “stellar” model space, and was in fact obtained during an earlier iteration of our Bayesian sampling. The simulation of F07 is obtained with a slightly different form of the galaxy potential, but is otherwise similar to a state within our current model. However, the stream velocities in this simulation are too high by about 50 km s^{-1} on average, a deficiency remedied by the larger values of M_{200} in the current samples. Mori & Rich (2008) used a live M31 model in three simulations that otherwise followed the general pattern of the F07 model. Without direct constraints from the star-count map, these models and the earlier ones of Fardal et al. (2006) used a much larger trial range of physical parameters such as M_{sat} than shown to be allowed in this paper.

The results in Section 3 assign the GSS progenitor a stellar mass of $(3.7 \pm 0.7) \times 10^9 M_{\odot}$. This mass is just about equal to that of the LMC, according to the model of van der Marel et al. (2002). Thus the GSS progenitor was either the fourth or fifth most massive galaxy in the Local Group as recently as 1 Gyr ago. Using simple estimates for a 10 Gyr stellar population, we find a V luminosity about a factor of 3 lower than the LMC, due to a higher M/L than expected for the actively star-forming LMC population.

Is our stellar mass reasonable? We can check this by means of the stellar metallicity in the GSS, estimated in several datasets to be in the range $[\text{Fe}/\text{H}] = -0.7$ to -0.5 within the GSS (Guhathakurta et al. 2006; Brown et al. 2006; Ibata et al. 2007; Gilbert et al. 2009). Using a solar metal fraction of $Z_{\odot} = 0.019$, this translates to $\log_{10} Z \approx -2.3$, which is well within the trend of stellar metallicities shown by local galaxies at our derived mass (Dekel & Woo 2003; Woo et al. 2008).

The dark matter in the progenitor is less well constrained by our modeling. Limits on the heating of M31’s disk place an upper limit on the GSS progenitor’s mass of about $5 \times 10^9 M_{\odot}$ (Mori & Rich 2008). In addition, the stream velocity dispersion constraints in Figure 7 independently suggest a mass of $\lesssim 10^{10} M_{\odot}$. Therefore we have less than a factor of two room for dark matter mass in the progenitor at the time of disruption. This is not as implausible as it may seem. A baryonic/dark mass ratio of $\lesssim 2$ within the main body of the galaxy is reasonable for galaxies of this mass (e.g., van der Marel et al. 2002). We infer that the bulk of the original dark matter associated with the progenitor, most of which must have extended beyond its stellar body, was stripped off in previous orbits.

The picture of multiple encounters with M31 agrees with the orbits derived from our modeling, which place the apocenter well within M31’s virial radius. Several orbital passes are probably necessary to lose enough energy and angular momentum to shrink the orbit and allow a final disruptive pericentric passage. It is possible that interactions with massive third bodies such as M33 may play a role as well.

According to our model, the disruptive pericentric pas-

sage that formed the GSS took place 760 ± 50 Myr ago, small in cosmological terms. This is much more recent than the last clear period of star formation ($\sim 4\text{--}5$ Gyr) found from modeling of HST/ACS data on the GSS down to the main sequence in Brown et al. (2006). We ascribe this to an earlier ram-pressure stripping of the GSS’s interstellar medium, which would imply a hot halo in M31. On the other hand, the model puts this disruptive encounter much too far in the past to induce the expanding star-forming wave that Block et al. (2006) envisioned to explain the 10 kpc ring of star formation in M31. That model fairly reliably requires a collision 210 Myr ago, since the outward propagation speed of the star-forming wave in this model is closely tied to M31’s accurately known rotation curve.

Our model still has certain deficiencies, notably the transverse distribution in the stream. We have previously argued that the transverse distribution is best explained with a rotating progenitor (Fardal et al. 2008). When it comes to a complex phenomenon such as the GSS merger, of course, it is likely that all models be will wrong on some level; the question is whether the disagreement indicates an uninteresting discrepancy, an interesting direction in which the model could be improved, or a serious flaw indicating the model is fundamentally wrong. The generally good agreement with a complex set of observational data indicates to us the model is generally plausible at this point. Any alternative model for the stream should be compared to data at a similar level of detail before it can be considered viable. Forthcoming wider-field data from the PAndAS survey can be used to refine the observational input, in part by better assessing the background contamination model. That survey may also show signs of a more complex initial structure than our simple Plummer model, such as remnants of a disk which may form cold arc-like features, or remnants of a halo which might have been stripped off in earlier encounters with M31. New spectroscopic samples of RGB stars, when compared to our libraries of fairly sampled simulations, can also be used to test the model further in the near future.

4.3 M31’s halo mass

Our models find the halo mass to be $\log_{10}(M_{200}/M_{\odot}) = 12.27 \pm 0.10$. Translating this to a threshold commonly used to represent the virial density, 100 times the critical or about 400 times the background density, gives $\log_{10}(M_{100}/M_{\odot}) = 12.33 \pm 0.10$, or $M_{100} = (2.1 \pm 0.5) \times 10^{12} M_{\odot}$.

In the following discussion, for consistency with most of the cosmological literature, we translate to a “virial” mass defined by M_{100} as opposed to M_{200} . We also use approximate translations between mass measures suggested by our observationally-constrained mass model of M31. (See van der Marel et al. 2012 for a discussion that covers some of the same issues, but assigns different emphasis to various methods of measuring mass.)

Earlier work has exhibited tension between observational measures of M31’s stellar and halo mass on the one hand, and expectations from the general galactic population and Local Group-based dynamical arguments on the other. For example, using a set of dynamical tracers in the outskirts of M31, Evans et al. (2000) found a total mass of $0.7\text{--}1.0 \times 10^{12} M_{\odot}$.

The models of Widrow et al. (2003) that use an NFW

halo imply a virial mass $M_{100} = 0.9\text{--}1.5 \times 10^{12} M_{\odot}$. Using orbital fits to the GSS, Ibata et al. (2004) found a mass within 125 kpc of only $0.75_{-0.13}^{+0.25} \times 10^{12} M_{\odot}$, suggesting a virial mass of $(1.0 \pm 0.5) \times 10^{12} M_{\odot}$. Seigar et al. (2008) found a virial mass of $0.82 \times 10^{12} M_{\odot}$ by fitting M31's rotation curve with a model of adiabatic contraction. Geehan et al. (2006) inferred a virial mass of $0.77 \times 10^{12} M_{\odot}$. Watkins et al. (2010) used tracer mass formulae and data on the dSph population to estimate M31's mass within 300 kpc as $(0.85 \pm 0.24) \times 10^{12} M_{\odot}$ to $(1.6 \pm 0.4) \times 10^{12} M_{\odot}$, depending on which galaxies were assumed to be virialized and other assumptions. These values suggest virial masses of $(0.77 \pm 0.25) \times 10^{12} M_{\odot}$ to $(1.6 \pm 0.5) \times 10^{12} M_{\odot}$. There are several uncertainties not incorporated in the Watkins estimates, for example the effect of the satellite density slope (taken to be -2.1 in Watkins but estimated as about -1.0 in Richardson et al. 2011). A similar calculation using globular clusters instead of dSph yielded $(1.2 \pm 0.2) \times 10^{12} M_{\odot}$ to $(1.5 \pm 0.2) \times 10^{12} M_{\odot}$ within 200 kpc, depending on the slope of the assumed potential Veljanoski et al. (2013). It is likely that most of the above studies have failed to include some important systematics in the error estimate. We also note that several methods are drawing upon similar datasets, for example those that use satellites as tracers, so the estimates are not independent.

Estimates of the stellar mass in the bulge and disk include $9.5 \times 10^{10} M_{\odot}$ (Widrow et al. 2003), $10.4 \times 10^{10} M_{\odot}$ (Geehan et al. 2006), $11.4 \times 10^{10} M_{\odot}$ (Seigar et al. 2008), and $10.1 \times 10^{10} M_{\odot}$ (?). This implies that stars constitute about half of M31's halo baryons, with estimates ranging as high as 86% (Geehan et al. 2006), if we assume a virial mass $10^{12} M_{\odot}$ and a cosmic baryon to total matter ratio $\Omega_b/\Omega_m \approx 0.15$.

These high stellar fractions conflict with values inferred from halo abundance matching and related techniques, where surveys of the general galactic population are compared with the expected halo and subhalo mass distribution in an LCDM cosmology. These methods suggest the stars of central halo galaxies take up only 10–20% of the halo baryons on average, (e.g. Guo et al. 2010; Behroozi et al. 2010), even at the halo mass corresponding to peak efficiency. For a M31 stellar mass of $0.10 \times 10^{12} M_{\odot}$, in line the estimates given earlier, the formula in Guo et al. (2010) converted to virial mass gives an M31 virial mass of about $7.4 \times 10^{12} M_{\odot}$, far above the observational estimates of M31 halo masses.

This tension echoes a current puzzle about the Milky Way, which also by some measures has a low estimated halo mass for its stellar mass. For example, using halo star velocities Xue et al. (2008) estimate a virial mass $(1.0 \pm 0.3) \times 10^{12} M_{\odot}$. Smith et al. (2007) estimate the local escape velocity and thereby a virial mass of $1.4_{-0.54}^{+1.14} \times 10^{12} M_{\odot}$. In contrast, a halo mass of $2.0 \times 10^{12} M_{\odot}$ would be most appropriate for a stellar mass of about $5.5 \times 10^{10} M_{\odot}$ (Guo et al. 2010). It would be very strange to have both large Local Group galaxies lie far off the typical stellar-halo mass trend. Also, the classical timing argument for the local group (Kahn & Woltjer 1959) suggests the M31 and the MW virial masses combine to $5.2 \times 10^{12} M_{\odot}$ (Li & White 2008) to $(4.9 \pm 1.6) \times 10^{12} M_{\odot}$ (van der Marel et al. 2012), about twice the sum of the typical observational estimates given

earlier (although the uncertainty in this mass is large and that of M31 as derived from this method is even larger).

We now reconsider the problem, using our new, higher estimate of M31's halo mass. First we re-estimate the baryonic mass of M31, using the value of $L_K = 13.7 \times 10^{10}$ derived from the Spitzer $3.6\mu\text{m}$ luminosity and estimated $K - [3.6]$ color in Barmby et al. (2006). Using the typical value of $B - R \approx 1.5$ as in Barmby et al, we find $M/L_K = 0.62$ based on Bell et al. (2003) using their stated correction term of -0.15 dex to translate to a Kroupa (2001) initial mass function. This yields a stellar mass of $8.6 \times 10^{10} M_{\odot}$ for M31.

We can only expect the M31 and MW estimates to be consistent with halo abundance matching if there is some scatter in the relationship between halo mass and stellar mass. Various arguments lead to a scatter of $\sigma_* \sim 0.1$ dex, which is explicitly modeled in Yang et al. (2009) and Behroozi et al. (2010) among others. The virial masses yielding a median stellar mass of $8.6 \times 10^{10} M_{\odot}$ are $5.0 \times 10^{12} M_{\odot}$ and $7.6 \times 10^{12} M_{\odot}$ respectively using results from these two papers.

However, when inverting the relationship to get the median halo mass at a given stellar mass, we should take account of the halo luminosity function, which lowers this median since there are many more low-mass than high-mass halos. We can treat this with a simple approximation. Using the assumed Gaussian distribution in $\log_{10} M_*$, assuming a power-law halo mass function $dN/d\log_{10} M_h \propto M_h^{-\gamma}$ with $\gamma \approx 0.9$ (e.g. Tinker et al. 2008), and taking a local power-law relationship $M_* \propto M_h^{\beta}$, we find an offset of $-\gamma \ln(10) \sigma_*^2 \beta^{-2}$. The distribution will be a Gaussian in $\log_{10} M_*$ with dispersion $\beta^{-1} \sigma_*$.

We find the final distributions in $\log_{10} M_h$ have means and dispersions (12.55, 0.25) for the data given in Yang et al. (2009), and (12.57, 0.40) for the data given in Behroozi et al. (2010). Uncertainty in the stellar mass adds to the intrinsic dispersion, implying the uncertainty in the halo mass may be even larger than given here. Our best value of $\log_{10} M_h = 12.33 \pm 0.10$ sits comfortably within these distributions.

Our detailed fitting of the GSS thus alleviates the tension between M31's halo mass and the general galaxy population. Of course, it is too early to consider this issue definitively settled. A host of systematic effects not considered here may bias our result. Ones that may prove significant include dynamical friction, errors in the assumed M31 distance, asphericity of the halo potential, and deviations of the potential shape from our simple one-parameter family. However, our result does illustrate the potential of the simulation sampling method. The presence of several long streams in the PAndAS survey (McConnachie et al. 2009) suggests we can reduce both statistical errors and degeneracies by applying constraints from several objects simultaneously, which is quite feasible within a Bayesian framework.

5 CONCLUSIONS

We have combined N-body models of the Giant Southern Stream (GSS) and related debris structures within M31 with MCMC sampling methods, to describe our knowledge of the interesting physical parameters. We have added the sky pattern of RGB stars, as given by the INT photometric survey

of M31's halo, to the observations of GSS positional and kinematic quantities used in previous stream fitting work. The combination of observables now tightly constrains the model.

We find the stream's progenitor had a stellar mass at last pericentric passage of $\log_{10}(M_s/M_\odot) = 9.5 \pm 0.1$, comparable to the LMC. The time of this disruptive pericentric passage is tightly constrained to 760 ± 50 Myr. Several lines of evidence suggest that the mass of dark matter in the progenitor was, at most, similar to the stellar mass. We expect the debris from the progenitor's core to be located in the NE Shelf. Characteristic signatures in the space of velocity versus radius may help localize the core debris in kinematic surveys. We find M31's virial mass is $\log_{10} M_{200} = 12.3 \pm 0.1$, alleviating the previous tension between observational virial mass estimates and expectations from the general galactic population and the timing argument.

More generally, we expect the techniques used in this paper to be useful in building informative models of other tidal debris structures. The combination of Bayesian methods with N -body simulation requires significant investments of both computer time and human effort. Future work will surely yield technical advances on the sampling techniques used here, and we have indicated some possible directions for study. However, even at the current level of sophistication, the rewards of the method are significant, including libraries of fairly sampled simulations and uncertainty estimates of physical parameters that allow for scientifically meaningful discussion.

ACKNOWLEDGMENTS

We thank Tom Quinn and Joachim Stadel for the use of PKDGRAV, and Josh Barnes for the use of ZENO. MAF and MDW acknowledge support by NSF grant AST-1009652 to the University of Massachusetts. AB acknowledges support from NSERC through the Discovery Grant program. PG acknowledges support by NSF grant AST-1010039 and NASA grant HST-GO-12055. KG acknowledges support from NASA through Hubble Fellowship grant 51273.01 by the Space Telescope Science Institute, which is operated by the Association of Universities for Research in Astronomy, Inc., for NASA, under contract NAS 5-26555. We acknowledge useful conversations with Anil Seth, Elena d'Onghia, and John Dubinski.

REFERENCES

Abadi M. G., Navarro J. F., Steinmetz M., 2006, *MNRAS*, 365, 747
 Aparicio A., Gallart C., 2004, *AJ*, 128, 1465
 Barmby P., Ashby M. L. N., Bianchi L., Engelbracht C. W., Gehrz R. D., Gordon K. D., Hinz J. L., Huchra J. P., Humphreys R. M., Pahre M. A., Pérez-González P. G., Polonski E. F., Rieke G. H., Thilker D. A., Willner S. P., Woodward C. E., 2006, *ApJ*, 650, L45
 Beaumont M. A., 2010, *Annual Review of Ecology, Evolution, and Systematics*, 41, 379
 Behroozi P. S., Conroy C., Wechsler R. H., 2010, *ApJ*, 717, 379
 Bell E. F., de Jong R. S., 2001, *ApJ*, 550, 212

Bell E. F., McIntosh D. H., Katz N., Weinberg M. D., 2003, *ApJS*, 149, 289
 Block D. L., Bournaud F., Combes F., Groess R., Barmby P., Ashby M. L. N., Fazio G. G., Pahre M. A., Willner S. P., 2006, *Nat*, 443, 832
 Bower R. G., Vernon I., Goldstein M., Benson A. J., Lacey C. G., Baugh C. M., Cole S., Frenk C. S., 2010, *MNRAS*, 407, 2017
 Brainerd T. G., Specian M. A., 2003, *ApJ*, 593, L7
 Brown T. M., Smith E., Ferguson H. C., Rich R. M., Guhathakurta P., Renzini A., Sweigart A. V., Kimble R. A., 2006, *ApJ*, 652, 323
 Brown T. M., Smith E., Guhathakurta P., Rich R. M., Ferguson H. C., Renzini A., Sweigart A. V., Kimble R. A., 2006, *ApJ*, 636, L89
 Bullock J. S., Johnston K. V., 2005, *ApJ*, 635, 931
 Carlberg R. G., 2009, *ApJ*, 705, L223
 Chapman S. C., Ibata R., Irwin M., Koch A., Letarte B., Martin N., Collins M., Lewis G. F., McConnachie A., Peñarrubia J., Rich R. M., Trethewey D., Ferguson A., Huxor A., Tanvir N., 2008, *MNRAS*, 390, 1437
 Conn A. R., Ibata R. A., Lewis G. F., Parker Q. A., Zucker D. B., Martin N. F., McConnachie A. W., Irwin M. J., Tanvir N., Fardal M. A., Ferguson A. M. N., Chapman S. C., Valls-Gabaud D., 2012, *ApJ*, 758, 11
 Cooper A. P., Cole S., Frenk C. S., White S. D. M., Helly J., Benson A. J., De Lucia G., Helmi A., Jenkins A., Navarro J. F., Springel V., Wang J., 2010, *MNRAS*, 406, 744
 Davidge T. J., 2012, *ApJ*, 749, L7
 de Vaucouleurs G., de Vaucouleurs A., Corwin Jr. H. G., Buta R. J., Paturel G., Fouque P., 1991, *Third Reference Catalogue of Bright Galaxies*
 Dekel A., Woo J., 2003, *MNRAS*, 344, 1131
 Evans N. W., Wilkinson M. I., 2000, *MNRAS*, 316, 929
 Evans N. W., Wilkinson M. I., Guhathakurta P., Grebel E. K., Vogt S. S., 2000, *ApJ*, 540, L9
 Eyre A., Binney J., 2011, *MNRAS*, 413, 1852
 Fardal M. A., Babul A., Geehan J. J., Guhathakurta P., 2006, *MNRAS*, 366, 1012
 Fardal M. A., Babul A., Guhathakurta P., Gilbert K. M., Dodge C., 2008, *ApJ*, 682, L33
 Fardal M. A., Guhathakurta P., Babul A., McConnachie A. W., 2007, *MNRAS*, 380, 15
 Fardal M. A., Guhathakurta P., Gilbert K. M., Tollerud E. J., Kalirai J. S., Tanaka M., Beaton R., Chiba M., Komiyama Y., Iye M., 2012, *MNRAS*, 423, 3134
 Ferguson A. M. N., Irwin M. J., Ibata R. A., Lewis G. F., Tanvir N. R., 2002, *AJ*, 124, 1452
 Flury T., Shephard N., 2011, *Econometric Theory*, 27, 933
 Font A. S., Johnston K. V., Ferguson A. M. N., Bullock J. S., Robertson B. E., Tumlinson J., Guhathakurta P., 2008, *ApJ*, 673, 215
 Font A. S., Johnston K. V., Guhathakurta P., Majewski S. R., Rich R. M., 2006, *AJ*, 131, 1436
 Geehan J. J., Fardal M. A., Babul A., Guhathakurta P., 2006, *MNRAS*, 366, 996
 Gelman A., Carlin J. B., Stern H. S., Rubin D. B., 2003, *Bayesian Data Analysis, Second Edition (Texts in Statistical Science)*, 2 edn. Chapman & Hall/CRC
 Gilbert K. M., Fardal M., Kalirai J. S., Guhathakurta P., Geha M. C., Isler J., Majewski S. R., Ostheimer J. C., Patterson R. J., Reitzel D. B., Kirby E., Cooper M. C.,

- 2007, *ApJ*, 668, 245
- Gilbert K. M., Font A. S., Johnston K. V., Guhathakurta P., 2009, *ApJ*, 701, 776
- Gilbert K. M., Guhathakurta P., Kollipara P., Beaton R. L., Geha M. C., Kalirai J. S., Kirby E. N., Majewski S. R., Patterson R. J., 2009, *ApJ*, 705, 1275
- Grillmair C. J., 2009, *ApJ*, 693, 1118
- Guhathakurta P., Rich R. M., Reitzel D. B., Cooper M. C., Gilbert K. M., Majewski S. R., Ostheimer J. C., Geha M. C., Johnston K. V., Patterson R. J., 2006, *AJ*, 131, 2497
- Guo Q., White S., Li C., Boylan-Kolchin M., 2010, *MNRAS*, 404, 1111
- Helmi A., 2004, *ApJ*, 610, L97
- Howley K. M., Geha M., Guhathakurta P., Montgomery R. M., Laughlin G., Johnston K. V., 2008, *ApJ*, 683, 722
- Ibata R., Chapman S., Ferguson A. M. N., Irwin M., Lewis G., McConnachie A., 2004, *MNRAS*, 351, 117
- Ibata R., Chapman S., Ferguson A. M. N., Lewis G., Irwin M., Tanvir N., 2005, *ApJ*, 634, 287
- Ibata R., Irwin M., Lewis G., Ferguson A. M. N., Tanvir N., 2001, *Nat*, 412, 49
- Ibata R., Martin N. F., Irwin M., Chapman S., Ferguson A. M. N., Lewis G. F., McConnachie A. W., 2007, *ApJ*, 671, 1591
- Irwin M., Lewis J., 2001, *New Astron. Rev.*, 45, 105
- Irwin M. J., Ferguson A. M. N., Ibata R. A., Lewis G. F., Tanvir N. R., 2005, *ApJ*, 628, L105
- Johnson V. E., 2005, *ArXiv Mathematics e-prints*
- Johnston K. V., 1998, *ApJ*, 495, 297
- Johnston K. V., Bullock J. S., Sharma S., Font A., Robertson B. E., Leitner S. N., 2008, *ApJ*, 689, 936
- Johnston K. V., Law D. R., Majewski S. R., 2005, *ApJ*, 619, 800
- Johnston K. V., Spergel D. N., Haydn C., 2002, *ApJ*, 570, 656
- Kahn F. D., Woltjer L., 1959, *ApJ*, 130, 705
- Kalirai J. S., Guhathakurta P., Gilbert K. M., Reitzel D. B., Majewski S. R., Rich R. M., Cooper M. C., 2006, *ApJ*, 641, 268
- Koposov S. E., Rix H., Hogg D. W., 2010, *ApJ*, 712, 260
- Kroupa P., 2001, *MNRAS*, 322, 231
- Law D. R., Majewski S. R., Johnston K. V., 2009, *ApJ*, 703, L67
- Li Y., White S. D. M., 2008, *MNRAS*, 384, 1459
- Libeskind N. I., Knebe A., Hoffman Y., Gottlöber S., Yepes G., 2011, *MNRAS*, 418, 336
- Mandelbaum R., Seljak U., Kauffmann G., Hirata C. M., Brinkmann J., 2006, *MNRAS*, 368, 715
- Martínez-Delgado D., Peñarrubia J., Gabany R. J., Trujillo I., Majewski S. R., Pohlen M., 2008, *ApJ*, 689, 184
- Martínez-Delgado D., Pohlen M., Gabany R. J., Majewski S. R., Peñarrubia J., Palma C., 2009, *ApJ*, 692, 955
- McConnachie A. W., et al., 2009, *Nat*, 461, 66
- McConnachie A. W., Irwin M. J., 2006, *MNRAS*, 365, 1263
- McConnachie A. W., Irwin M. J., Ferguson A. M. N., Ibata R. A., Lewis G. F., Tanvir N., 2005, *MNRAS*, 356, 979
- McConnachie A. W., Irwin M. J., Ibata R. A., Ferguson A. M. N., Lewis G. F., Tanvir N., 2003, *MNRAS*, 343, 1335
- Merrett H. R., Merrifield M. R., Douglas N. G., Kuijken K., Romanowsky A. J., Napolitano N. R., Arnaboldi M., Capaccioli M., Freeman K. C., Gerhard O., Coccato L., Carter D., Evans N. W., Wilkinson M. I., Halliday C., Bridges T. J., 2006, *MNRAS*, 369, 120
- Merrifield M. R., Kuijken K., 1998, *MNRAS*, 297, 1292
- More S., van den Bosch F. C., Cacciato M., Mo H. J., Yang X., Li R., 2009, *MNRAS*, 392, 801
- Mori M., Rich R. M., 2008, *ApJ*, 674, L77
- Press W. H., Teukolsky S. A., Vetterling W. T., Flannery B. P., 2007, *Numerical Recipes*, third edn. C. Cambridge University Press
- Pritchett C. J., van den Bergh S., 1994, *AJ*, 107, 1730
- Richardson J. C., Ferguson A. M. N., Johnson R. A., Irwin M. J., Tanvir N. R., Faria D. C., Ibata R. A., Johnston K. V., Lewis G. F., McConnachie A. W., Chapman S. C., 2008, *AJ*, 135, 1998
- Richardson J. C., Irwin M. J., McConnachie A. W., Ibata R. A., Chapman S. C., Lewis G. F., Tanvir N. R., Rich R. M., 2011, *ApJ*, 732, 76
- Schlegel D. J., Finkbeiner D. P., Davis M., 1998, *ApJ*, 500, 525
- Searle L., Zinn R., 1978, *ApJ*, 225, 357
- Seigar M. S., Barth A. J., Bullock J. S., 2008, *MNRAS*, 389, 1911
- Smith M. C., Ruchi G. R., Helmi A., Wyse R. F. G., Fulbright J. P., Freeman K. C., Navarro J. F. e., 2007, *MNRAS*, 379, 755
- Stadel J. G., 2001, PhD thesis, UNIVERSITY OF WASHINGTON
- Tanaka M., Chiba M., Komiyama Y., Guhathakurta P., Kalirai J. S., Iye M., 2010, *ApJ*, 708, 1168
- Ter Braak C. J. F., 2006, *Statistics and Computing*, 16, 239
- Theis C., Kohle S., 2001, *A&A*, 370, 365
- Tinker J., Kravtsov A. V., Klypin A., Abazajian K., Warren M., Yepes G., Gottlöber S., Holz D. E., 2008, *ApJ*, 688, 709
- van der Marel R. P., Alves D. R., Hardy E., Suntzeff N. B., 2002, *AJ*, 124, 2639
- van der Marel R. P., Fardal M., Besla G., Beaton R. L., Sohn S. T., Anderson J., Brown T., Guhathakurta P., 2012, *ApJ*, 753, 8
- Varghese A., Ibata R., Lewis G. F., 2011, *MNRAS*, 417, 198
- Veljanoski J., Ferguson A. M. N., Mackey A. D., Huxor A. P., Irwin M. J., Côté P., Tanvir N. R., Bernard E. J., Chapman S. C., Ibata R. A., Fardal M., Lewis G. F., Martin N. F., McConnachie A., Peñarrubia J., 2013, *ApJ*, 768, L33
- Watkins L. L., Evans N. W., An J. H., 2010, *MNRAS*, 406, 264
- Weinberg M. D., 2012a, *ArXiv e-prints*
- Weinberg M. D., 2012b, *Bayesian Analysis*, 07, 737
- Widrow L. M., Perrett K. M., Suyu S. H., 2003, *ApJ*, 588, 311
- Willett B. A., Newberg H. J., Zhang H., Yanny B., Beers T. C., 2009, *ApJ*, 697, 207
- Woo J., Courteau S., Dekel A., 2008, *MNRAS*, 390, 1453
- Xue X. X., Rix H. W., Zhao G., Re Fiorentin P., Naab T., Steinmetz M., van den Bosch F. C., Beers T. C., Lee Y. S., Bell E. F., Rockosi C., Yanny B., Newberg H., Wilhelm R., Kang X., Smith M. C., Schneider D. P., 2008, *ApJ*, 684, 1143

Yang X., Mo H. J., van den Bosch F. C., 2009, ApJ, 695,
900